Final Degree Project

Biomedical Engineering Degree

Automatic Feature Extraction Pipeline for Abdominal Aortic Aneurysm Characterization

Barcelona, 11th June, 2025

Author: Júlia Vila Delgado

Director/s: Dr. Josep Munuera & Ager Uribezubia

Tutor: Dr. Roser Sala

ACKNOWLEDGMENTS

The completion of this project would not have been possible without the help and support I received throughout its development.

First, I would like to give my sincere thanks to Ager Uribezubia for his ongoing guidance and support throughout the entire project. I would also like to thank Dr. Josep Munuera for giving me the opportunity to be part of this project and for trusting my work. I am also grateful to César Acebes and the Dimension Lab team, whose help and advice allowed me to solve several challenges along the way. Finally, I want to thank my family and friends for always being there for me, giving me support, encouragement, and motivation throughout this journey. Thank you all for making this project possible.

ABSTRACT

Abdominal Aortic Aneurysm (AAA) is a life-threatening vascular pathology whose diagnosis and follow-up rely primarily on maximum aortic diameter measurements from rudimentary CT scans. However, this metric presents important limitations, failing to capture the full morphological and pathological complexity of the aneurysm. This final degree thesis presents the design and validation of a fully automated pipeline for the extraction of morphological and radiomic features from contrast-enhanced CT scans of patients with AAA. The pipeline includes preprocessing, standardized segmentation, geometric and radiomic quantification, and report generation. Key features include tortuosity, curvature, cross-sectional areas, circularity, volume metrics, calcification analysis, thrombus-wall contact area and first and second order radiomic descriptors. The method was validated in a sample of ten patients from the Triple A Barcelona Study (TABS), allowing comparison between slow and fast growth aneurysms across two timepoints. Results showed strong correlation with manual diameter measurements (Pearson R = 0.98), and exploratory analyses revealed additional patterns potentially relevant for clinical assessment, such as internal thrombus remodeling or increased volumes in rapid-growth cases. Despite limitations related to sample size and manual segmentation, this work demonstrates the feasibility and robustness of a scalable, reproducible, and clinically oriented image analysis pipeline. It supports the integration of advanced imaging biomarkers into AAA evaluation, addressing current gaps in risk stratification and enabling future integration with omics data and AI-based tools. This approach contributes to a more comprehensive and personalized understanding of AAA progression beyond conventional diameter-based criteria.

Keywords: Abdominal Aortic Aneurysm – Feature Extraction – Computed Tomography – Segmentation – Automated Morphological Analysis – Shape Descriptors – Radiomic Features – Medical Imaging.

ABSTRACTE

L'aneurisma d'aorta abdominal (AAA) és una patologia vascular potencialment mortal, el diagnòstic i seguiment de la qual es basen principalment en la mesura manual del diàmetre màxim de l'aorta a partir de les imatges de TC. Tanmateix, aquest indicador presenta limitacions, ja que no capta la complexitat morfològica i patològica de l'aneurisma. Aquest treball presenta el disseny i la validació d'un pipeline automatitzat per a l'extracció de característiques morfològiques i radiòmiques a partir de tomografies computades de pacients amb AAA. El pipeline inclou preprocessament, segmentació estandarditzada, quantificació geomètrica i radiòmica, i generació d'informes. Entre les característiques clau s'hi troben la tortuositat, curvatura, àrees transversals, circularitat, volums, calcificacions, àrees de contacte, i descriptors radiòmics de primer i segon ordre. El mètode s'ha validat en una mostra de deu pacients de l'estudi Triple A Barcelona (TABS), permetent la comparació entre aneurismes de creixement lent i ràpid. Els resultats van mostrar una forta correlació amb les mesures manuals del diàmetre (Pearson R = 0.98), i les anàlisis exploratòries van revelar patrons potencialment rellevants per a l'avaluació clínica, com el remodelat intern del trombe o l'augment de volums en els casos de creixement ràpid. Malgrat les limitacions relacionades amb la mida de la mostra i la segmentació manual, aquest treball demostra la viabilitat i robustesa d'un pipeline d'anàlisi d'imatge escalable, reproduïble i orientat a l'àmbit clínic, capaç d'integrar biomarcadors d'imatge i contribuint a una comprensió més personalitzada de la progressió de l'AAA més enllà del diàmetre.

Paraules clau: Aneurisma de l'Aorta Abdominal – Extracció de Característiques – Tomografia Computada – Segmentació – Anàlisi Morfològica Automatitzada – Descriptors de Forma – Característiques Radiòmiques – Imatge Mèdica.

LIST OF FIGURES

LIST OF TABLES

LIST OF EQUATIONS

GLOSSARY OF ABBREVIATIONS

AAA – Abdominal Aortic Aneurysm

ABR – Aneurysm Biomechanical Ratio

AI – Artificial Intelligence

CE – Conformité Européenne

CNN – Convolutional Neural Network

CT – Computed Tomography

DB - Database

DICOM – Digital Imaging and Communications in Medicine

EU – European Union

EVAR – Endovascular Aortic Repair

FEA – Finite Element Analysis

GDPR – General Data Protection Regulation

GLCM – Gray-Level Co-occurrence Matrix

GLDM – Gray-Level Dependence Matrix

GLRLM – Gray-Level Run Length Matrix

GLSZM – Gray-Level Size Zone Matrix

HIPAA – Health Insurance Portability and Accountability Act

ILT – Intraluminal Thrombus

IRA – Infrarenal Aorta

ISO – International Organization for Standardization

LOPDGDD – Ley Orgánica de Protección de Datos y Garantía de Derechos Digitales

MAPE – Mean Absolute Percentage Error

MAE – Mean Absolute Error

MDR – Medical Device Regulation

MRI – Magnetic Resonance Imaging

MPR – Multiplanar Reconstruction

NIfTI – Neuroimaging Informatics Technology Initiative

OSR – Open Surgical Repair

PET – Positron Emission Tomography

PERT – Program Evaluation and Review Technique

PVAT – Perivascular Adipose Tissue

PWS – Peak Wall Stress

PWRI – Peak Wall Rupture Index

RMSE – Root Mean Square Error

RNA – Ribonucleic Acid

ROI – Region of Interest

RPI – Rupture Potential Index

STD – Standard Deviation

SFCM - Shape Fuzzy C-Means

SRA – Suprarenal Aorta

SWOT – Strengths, Weaknesses, Opportunities and Threats

T1 – Acquisition at Timepoint 1

T2 – Acquisition at Timepoint 2

TABS – Triple A Barcelona Study

UGMC – Complex Disease Genomics Unit

US – Ultrasound

WBS – Work Breakdown Structure

TABLE OF CONTENTS

1. INTRODUCTION

Abdominal Aortic Aneurysm (AAA) is a life-threatening condition characterized by the pathological dilation of the abdominal aorta, most often diagnosed when the maximum diameter exceeds 30 mm [1]. Though typically asymptomatic until rupture, AAA causes over 160,000 deaths annually worldwide, with extremely high post-rupture mortality rates exceeding 80% in many cases [1][2]. Current clinical practice highly relies on the measurement of the maximum aortic diameter as the primary indicator for diagnosis and treatment decisions. However, this metric has notable limitations, particularly in terms of predicting rupture risk and capturing the complex structural and pathological changes involved in aneurysm evolution.

In recent years, increasing attention has been given to the development of imaging biomarkers as complementary tools for disease stratification and management. Radiological biomarkers derived from medical images offer non-invasive, spatially resolved information that may reflect the underlying biomechanical stress, wall composition, or thrombus dynamics, factors that remain invisible to diameter-based assessments [3][4]. Moreover, the integration of computational tools for morphological and radiomic feature extraction is opening new possibilities in both research and clinical environments, with the potential to increase objectivity, reproducibility, and predictive value [5].

This final degree thesis focuses on the development of an automated pipeline to extract quantitative morphological and radiomic features from contrast-enhanced CT scans of patients with AAA. The goal is to explore whether these image-derived features can complement traditional measurements in terms of their relevance to disease assessment, prognosis, and ultimately, patient-specific management. The work is framed within the broader effort to transition from conventional radiological approaches to precision medicine in vascular pathology and aligns with current research trends emphasizing the need for comprehensive, reproducible, and scalable image analysis solutions.

1.1 Motivation and Origin of the Project

This project originates from the observed clinical and research limitations in the current methods to evaluate abdominal aortic aneurysms (AAA), particularly within the ongoing efforts of our research group to correlate omics data with anatomical and pathological features of the aneurysm. In these studies, the only available ground truth was the maximum diameter, manually measured by radiologists, an indicator widely used in clinical practice but with limitations in terms of predictive value and reproducibility.

Driven by the need to overcome these limitations and inspired by recent advances in medical image analysis, this project aims to provide a more complete AAA characterization through the automatic extraction of morphological and radiomic features from contrast-enhanced CT images. The idea arose from the observation that the aneurysm growing can occur in ways that do not always translate into diameter changes, such as longitudinal expansion or internal remodeling, which cannot be detected by traditional measurements.

This work aims to bridge the gap between classical radiological assessment and the demands of precision medicine, laying the groundwork for integrating image-based biomarkers into AAA research and management.

1.2 Objectives

The main goal of this thesis is to improve the characterization of the Abdominal Aortic Aneurysms integrating image processing techniques by extracting quantifiable properties from arterial phase CT scans through an automated algorithm. To achieve that, a detailed image processing pipeline will be developed and validated, aiming to provide significant insights about the disease's state and to evaluate its potential in clinical and research applications.

Based on this general objective, the following specific objectives are defined:

- **Review the state of the art:** Analyze recent techniques in image segmentation and image processing applied to the AAA study, with a focus on clinical and research environments.

- **Definition of structures of interest:** Determine which anatomical AAA regions and adjacent structures should be segmented for a significant disease evaluation.

- **Segmentation of the structures:** Implement a standardized segmentation method to segment the relevant structures from the CT images, validating the results with experimented radiologists.

- **Feature extraction:** Identify and extract quantifiable properties from the segmented images that reflect the physical and pathological state of the AAA.

- **Evaluation and comparison of results:** Compare the properties automatically extracted with traditional methods used in clinical practice, assessing their consistency and potential added value in disease analysis.

This project will serve as a proof of concept for the integration of image processing techniques in the AAA study, facilitating the development of automatized tools for its analysis and characterization.

1.3 Methodology

The methodology developed in this project is based in the creation of an automatic pipeline to extract morphological and radiomic features from contrast-enhanced CT scans of patients diagnosed with AAA.

The workflow has been divided into five main stages (*Figure 1*):
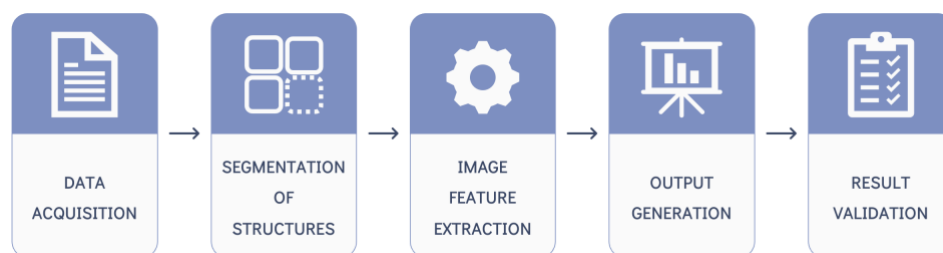
Figure 1: Main stages of the project workflow.

- **Data acquisition:** Collection of contrast-enhanced CT scans and selection of relevant patients.
- **Preprocessing and segmentation:** Segmentation of key anatomical structures.
- **Feature extraction:** Automatic computation of geometric and radiomic parameters.
- **Output generation:** Creation of summary tables and medical reports for result interpretation.
- **Result validation:** Comparison with manual measurements and analysis of result consistency.

All steps in the pipeline have been implemented using open-source tools, ensuring reproducibility by enabling future adaptation in both clinical and research settings. In addition, useful annexes are provided, and all the code implemented can be found in a public GitHub repository[1].

1.4 Limitations

Several limitations were found during the development of this project. First, the sample size was small, which limits statistical power and generalizability of the results. Second, the segmentation process was manual, introducing potential interobserver variability despite the use of standardized protocol. Third, image quality and acquisition parameters varied slightly between patients, which may have affected the consistency of certain measurements. Additionally, the pipeline was only validated technically and not clinically, so its integration into real clinical workflows requires further testing. Finally, time constraints limited the possibility of applying the method to a larger cohort or exploring advanced machine learning approaches.

1.5 Location

This project has been developed in collaboration with the Complex Disease Genomics Unit (UGMC) group at Institut de Recerca de l'Hospital de Sant Pau under the supervision of Josep Munuera (principal investigator) and Ager Uribezubia (PhD student).

2. BACKGROUND

To provide a comprehensive understanding of the clinical and technical context in which this project is framed, this section presents a detailed overview of the medical background of AAA and the imaging technologies used for their analysis.

2.1 Medical Background

2.1.1 The Aorta

The aorta is one of the main arteries in the human body. It is also the longest one, with an extension of approximately 2,5 cm of diameter in healthy adults. It originates in the left ventricle of the heart, it has an ascending initial trajectory, but then it creates an arch (aortic arch) and descends through the thorax until the abdomen. At this point, at the level of L4 vertebrae, it bifurcates into the left and right iliac arteries. Its main function is to transport oxygenated blood, rich in nutrients, to the body via the systemic circulation.

The aorta can be divided into four sections: the ascending aorta, the aortic arch, the thoracic (descending) aorta and the abdominal aorta [6].

---

[1] GitHub repository link: https://github.com/juliaviladelgado/TFG_AAA_Analysis

2.1.2 Abdominal Aorta

The abdominal aorta is a continuation of the thoracic aorta, and in adults, it usually has an extension of approximately 13 cm, ending at the level of the L4 vertebra, where it splits into the common iliac arteries.

In *Figure 2*, a normal anatomy of the aorta can be observed. It can also be seen that many branches arise from it. The ones considered most important and relevant for this project are the celiac trunk, right and left renal arteries and superior mesenteric artery.

These arteries are highlighted first, because they are the principal arteries supplying major abdominal organs, so changes in their permeability can directly influence aortic blood flow patterns. And secondly, their permeability status is also linked to the functional integrity of the organs they supply. For instance, renal artery occlusion can lead to kidney failure, and similarly, compromise in these vessels can have significant effects on the patient's overall health and prognosis.
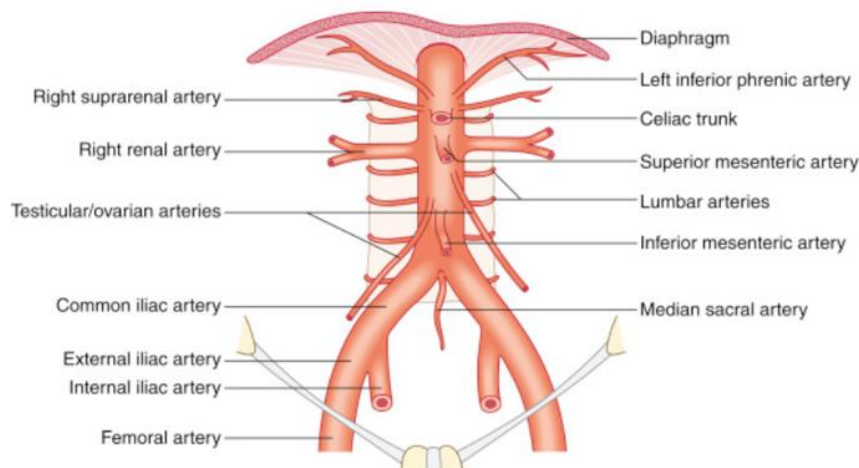
Figure 2: Branches of the abdominal aorta [7].

2.1.3 Abdominal Aortic Aneurysm (AAA)

Abdominal aortic aneurysms (AAA) are an enlargement of the abdominal section of the aorta caused by weakness in the artery walls under the pressure of blood flow (see *Figure 3*). In most cases, the disease is asymptomatic, as the aneurysm itself does not cause any pain and does not affect the patient's functionality, making it difficult to diagnose. Despite initially being asymptomatic, AAA represents significant danger as it cannot shrink but may continue to increase in size until it ruptures, leading to fatal consequences for the patient as the mortality rate is about 80-85% once the rupture occurs [8]. Aneurysms rupture occurs when the wall stress due to blood pressure exceeds the aortic wall strength. At this point, the aorta can no longer withstand the forces applied to it and it breaks [8].
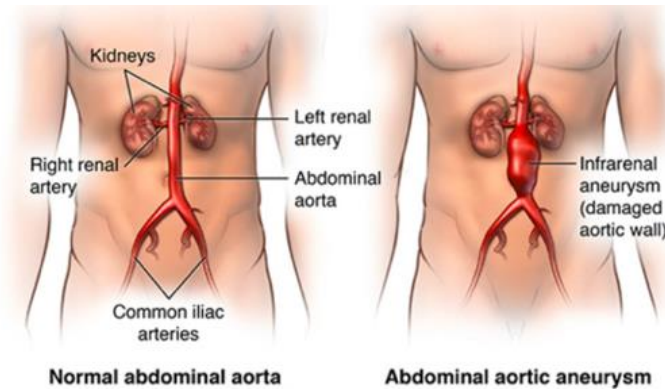
Figure 3: Abdominal Aortic Aneurysm representation [9].

2.1.3.1 Risk Factors

AAA causes approximately 170.000 deaths annually worldwide [1]. While usually it is an asymptomatic disease, there are some risk factors to be considered that influence its development. According to recent literature, the most relevant risk factors are [1] [10]:

- **Age**: The prevalence of AAA increases significantly with age, particularly in individuals over the age of 65, caused by degenerative changes in the vascular wall, contributing to aneurysm formation.
- **Sex**: AAA is substantially more common in males than females. Men have up to four times higher prevalence, though women tend to present with aneurysms at smaller diameters and experience higher risk of rupture when they occur.
- **Smoking**: Smoking is the most important modifiable risk factor. It contributes to vascular wall degradation and inflammation, significantly increasing the likelihood of aneurysm formation and growth.
- **Family history**: A genetic predisposition to AAA has been identified with individuals having a first-degree relative affected by the condition being at elevated risk.
- **Hypertension and other cardiovascular diseases**: High blood pressure and atherosclerosis are common in patients with AAA. These conditions weaken the vessel wall and contribute to aneurysm development and progression.

These risk factors are agreed within the clinical literature and play an important role in determining screening eligibility and monitoring protocols for patients.

2.1.3.2 Treatment Options for AAA

There exist several management options for AAA, depending on the aneurysm size, growth rate and presence of symptoms. Treatment strategies range from conservative surveillance to surgical intervention, aiming to prevent rupture, which carries a high mortality risk [11].

Conservative Management: Small, asymptomatic AAA (typically those with a diameter smaller than 5,5 cm in men or 5,0 cm in women) are generally managed with active surveillance rather than immediate surgery. This includes routine imaging follow-ups, lifestyle interventions and pharmacological control [10][11].

Surgical Repair: When the aneurysm exceeds the threshold for intervention (usually ≥5.5 cm in men or ≥5.0 cm in women), or in the presence of symptoms or rapid growth, surgical repair is indicated [11].

There are two primary surgical options:

- **Open Surgical Repair (OSR)** involves direct abdominal incision to remove the aneurysmal segment and replace it with a synthetic graft (*Figure 4, left)*. Though invasive, OSR offers long-term durability and may be preferred in younger and low-risk patients [11].
- **Endovascular Aortic Repair (EVAR)** uses minimally invasive approach in which a stent graft is inserted via femoral and positioned inside the aneurysm to exclude it from circulation (*Figure 4, right*). EVAR is associated with reduced short-term morbidity, quicker recovery and lower perioperative mortality compared to OSR, although it may require more frequent imaging follow-up due to risks such as endoleaks or graft migration [11].

The choice between EVAR and OSR depends on patient anatomy, comorbidities, life expectancy, and institutional expertise. However, despite improvements in cardiovascular risk factor management, 5-year survival after successful aneurysm repair remains below 70% [11].
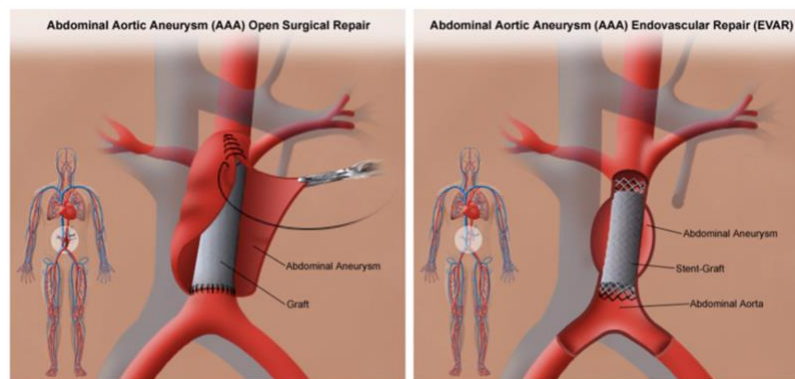
Figure 4: Open Surgical Repair (left) vs. Endovascular Aortic Repair (right) [12].

Emergency Treatment: In the event of ruptured AAA, emergency surgery (either OSR or EVAR) is essential. Despite advances in surgical techniques, the mortality rate remains high, emphasizing the importance of early detection and elective intervention [11]. Studies indicate that, in ruptured aneurysm patients, mortality in the postoperative days is around 35%. Moreover, in many cases, more than 50% of patients with rupture die before reaching the hospital [11].

2.2 Technical Background

2.2.1 Medical Imaging in AAA Diagnosis

Medical imaging plays a fundamental role in the diagnosis, monitoring, and treatment planning of many diseases in modern medicine, allowing to observe inside the body in a non-invasive way. There are different types of medical imaging, including X-rays, Computed Tomography (CT), Magnetic Resonance (MRI), Ultrasound (US) or Positron Emission Tomography (PET). These techniques provide detailed information about the organs, tissues, and blood vessels.

In the context of AAA, both CT and US are widely used in diagnostic imaging techniques. While CT is considered the gold standard due to its high resolution and 3D visualization capabilities, ultrasound is often the first choice for initial screening and follow-up of AAA because it is quick, inexpensive, and does not emit ionizing radiation. However, the effectiveness of ultrasound depends on the operator's skill, and typically does not provide image records like CT, limiting its value in quantitative studies or longitudinal follow-up.

The dataset used in this project consists of contrast-enhanced Computed Tomography (CT) images acquired from patients diagnosed with AAA. CT is a widely used medical imaging technique that provides cross-sectional images of the body and is considered one of the gold standards for assessing vascular pathologies, including aneurysms [13].

CT imaging operates by measuring the attenuation of X-rays as they pass through different tissues in the body. X-rays are a form of ionizing radiation that can penetrate the body to varying degrees depending on the density and composition of the tissues. Regions with a low density, such as air or fat, allow X-rays to pass through with minimal attenuation, resulting in darker regions on the final image. Conversely, tissues with higher density such as bone or calcified structures absorb more X-rays, producing brighter areas. This differential attenuation creates the contrast that enables the visualization of internal anatomical structures.

In CT, multiple X-ray projections are taken from different angles around the patient. These projections are then reconstructed using mathematical algorithms, such as filtered back projection or iterative reconstruction, to generate a volumetric dataset composed of thin axial slices. When these slices are combined, they provide a 3D representation of the anatomical region of interest, allowing localization and measurement of pathological features [14] *(Figure 5)*.
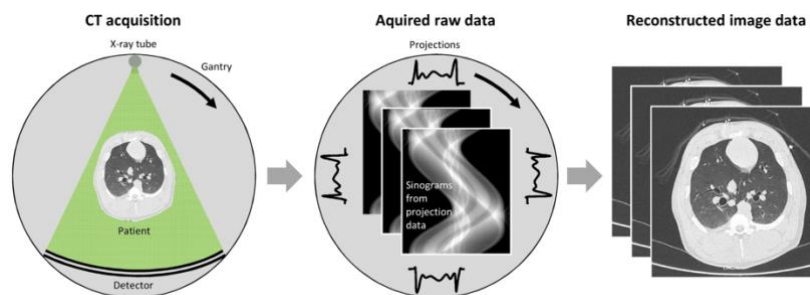
Figure 5: Computed Tomography (CT) acquisition workflow [14].

In the context of AAA, contrast-enhanced CT scans acquired during the arterial phase are particularly valuable. Intravenous contrast agents highlight the vascular lumen, delineating the aortic wall, and facilitating the location of intraluminal thrombus (ILT). These images enable assessment of the aneurysm's size, shape and relationship with surrounding branches, information that is essential for diagnosis, monitoring, and treatment planning.

2.2.2 Applications of Medical Imaging

CT scans are especially useful for looking at the shape and structure of the body. They create 3D images from many X-rays taken from different angles. These images help doctors and researchers

measure organs and identify problems. In research, CT images are also used for more advanced tasks like segmenting tissues, building 3D models, or simulating how blood flows through vessels.

One of the most common applications in AAA imaging is tissue segmentation, where different anatomical regions are automatically or manually delineated. The most common segmented structures in AAA are the aortic lumen, the intraluminal thrombus, and the aortic wall, which helps accurately measure the size and shape of the aneurysm to better understand the disease [8] [15].

These segmented images can also be used to obtain quantitative biomarkers, giving measurable characteristics of the image. Some examples are the thrombus volume, contact area between thrombus and wall or even the curvature of the vessel. Various studies are analyzing whether these biomarkers can better predict the rupture risk of the aneurysm than the maximum diameter alone, which is still the main clinical criteria used at present [1] [16].

Another relevant application is hemodynamic simulation, which allows to model the blood flow through the aneurysm using 3D models generated with images. This contributes to identify high stress zones in the aortic wall and understand how the disease evolves or when it could end up in rupture [10].

In recent years, artificial intelligence and automatic learning have also been applied to image analysis. These techniques can automatize processes such as segmentation, feature extraction or risk prediction. Deep learning models, like neural networks, show promising results in the automatic analysis of a big volume of medical images [10].

To sum up, medical images are no longer only a diagnostic tool. It allows to extract important data from the body, supporting clinical decisions and making possible the development of prediction models that can help improve sanitary attention, especially in diseases like AAA.

2.2.3 Quantitative Imaging

Quantitative imaging involves converting qualitative medical image data into objective measurable features that can provide clinically relevant information. By applying advanced computational methods, such as segmentation and feature extraction, it allows the analysis of anatomical and functional structures in a reproducible way, which is essential for research, diagnosis and treatment monitoring in AAA and other pathologies.

2.2.3.1 Image Format

The most used formats in medical imaging are DICOM (Digital Imaging and Communications in Medicine) and NIfTI (Neuroimaging Informatic Technology Initiative). DICOM is the clinical standard for managing, storing, and transmitting patient data, combining both the image and metadata, such as patient ID, modality, acquisition parameters, and spatial details like voxel spacing and slice thickness, within each file. However, because each slice is stored separately, DICOM is less suited for large scale computational workflows. To address this, images are often converted to NIfTI format, which consolidates volumetric data into a single file and includes a simpler header with key spatial metadata like voxel size and affine transformations, enabling more efficient processing and integration with Python-based tools [17]. During this conversion, anonymization is essential to meet

privacy laws such as the GDPR in Europe [18] and HIPAA in the US [19]. Tools that automate DICOM-to-NIfTI conversion often include options to strip personal identifiers, ensuring the resulting data is de-identified and ready to be used for research.

2.2.3.2 Image Processing Techniques

Image processing is a fundamental step in medical image analysis, allowing to transform raw imaging data into well-structured information, measurable and useful from a clinical point of view. These techniques are applied in various medicine areas and over different image modalities, such as CT, MRI, or echography, to help in diagnosis, disease progression and personalized treatment.

Some of the most common image operations include filtering (to reduce noise or improve contrast), registration (alignment of images taken at different moments in time or using different techniques) and resample (to ensure a good resolution and homogeneous orientations) [20]. These preprocessing steps are usually necessary before starting with more advanced steps.

One of the key techniques in medical image analysis is segmentation, which consists of identifying and isolating specific structures within the image, such as organs, tumors, blood vessels or lesions. Segmentation can be manual, semiautomatic, or automatic, and can use methods like thresholding, edge detection, region growing or model-based approaches [21]. In recent years, methods based on deep learning, especially convolutional neural networks (CNN) such as U-Net architecture, have gained widespread use in medical segmentation, offering a high precision and speed [22].

After segmentation, feature extraction stage starts, to quantify relevant properties from the detected structures. These characteristics can be geometrical, textural, or spatial. In many diseases these features are used as image biomarkers helping diagnostic, patient classification and the prediction or prognosis or the selection of the most appropriate treatment [23].

In the specific case for AAA, image processing techniques allow obtaining detailed anatomical information from contrast-enhanced CT scans. Once the aortic lumen and thrombus are segmented, techniques as centerline extraction, allow to compute metrics that quantify the morphological changes (tortuosity, curvature, transversal areas, and diameter profiles) along the aorta [24]. Furthermore, it is also possible to estimate the contact area between the thrombus and wall, a parameter related with biomechanical stress [25].

Moreover, the emerging field of radiomics allows to extract hundreds of quantitative characteristics from medical images, related to texture, shape and intensity statistics. These features can be used to develop predictive models that complement the current clinical criteria and help to create a more personalized medicine [23].

2.2.3.3 Structural Quantification

Structural quantification in medical imaging consists of the extraction and analysis of morphological characteristics that allow us to understand anatomical and pathological changes in diseases as AAA. These quantitative metrics include dimension measures (volume, surface area, diameters) and shape descriptors, such as tortuosity or curvature, which are critical for assessing disease evolution and risk [24]. Centerline extraction, allows for a more precise diameter profile and

tortuosity analysis, showing curvature and vessel deformation associated with aneurysm growth [25]. These quantitative parameters offer an added value for clinical evaluations that are more objective and reproducible and can back-up computational models for risk prediction.

2.2.3.4 Radiomic Quantification

Radiomics is an emerging field that enables the extraction of quantitative information from medical images to characterize biological processes in tissues and organs. It is based on the hypothesis that medical images capture subtle patterns related with the physiopathology of diseases, becoming a non-invasive "digital biopsy" [26].

Radiomic features are divided into different categories. First order features describe basic statistics based on pixel intensity. These metrics reflect a global distribution in intensity and provide a first approximation to homogeneity or heterogeneity of the lesion [27].

Second order features, such as grey-level co-occurrence matrices (GLCM), analyze spatial relationships between neighboring pixels and quantify texture patterns. Parameters like entropy or GLCM uniformity inform about complexity and internal lesion structure [27].

Higher order features (GLRLM, NGLDM) capture more complex relationships, like size of heterogeneous zones or intensity dependency with respect to distance and direction and can be associated with biological phenomena like vascularization, fibrosis, or necrosis presence [27].

Biologically radiomics aims to link these image-derived patterns to biological processes. For example, recent studies have shown how certain texture features extracted from the image correlate with tissue hypoxia, gene expression or immunological infiltration [26]. However, these relationships are still indirect and complex, and require for external validation [26].

In summary, radiomics enables to extract biomarkers that may provide added value to the diagnostic and prognostic in diseases like AAA. Its potential lies in the combination of spatial information, texture, and clinical data along with the biology related to the disease [26][27].

2.2.4 Clinical Importance of Advanced Techniques

The automation of medical image analysis, especially in the AAA study, can have a significative clinical impact. First, automatic methods allow to reduce diagnostic time. This is especially useful in clinical areas where a fast response is required [28].

Automation also contributes to create consistency and reproducibility among results, minimizing interobserver variability that usually appears in manual measurements. In the case of AAA, small differences in measurements can directly influence in important clinical decisions, such as the moment for surgical intervention [29].

In addition, advanced image processing techniques can provide support for clinicians by extracting biomarkers that go further the maximum diameter and will give more information. These include parietal stress, thrombus characteristics or geometrical descriptors, that allow for a more complete risk evaluation and a better patient stratification [15][23].

The integration of this tools in clinical practice can also facilitate personalized follow-ups, allowing tailored surveillance and control strategies according to the risk factors extracted from the image, instead of depending only on fixed size thresholds. Moreover, these techniques can help support presurgical planification, generating 3D models and spatial precise measures that contribute to improve security and efficiency of the procedure [24].

In summary, the use of advanced and automated techniques in the AAA analysis does not only improve efficiency and reduces variability, but also opens the door to more precise and tailored clinical decisions.

2.3 Research in AAA

Research in AAA has experienced a notable growing in last decades, focusing on morphological, biomechanical, and molecular aspects to improve diagnosis, risk stratification and therapeutical planning. Traditionally, transversal maximum diameter has been the main criteria to guide clinical decisions, but its limited predictive capacity has pushed the development of methods that integrate other types of parameters for a more precise evaluation [30][31]. Among these, morphological studies have explored three-dimensional geometry and thrombus characteristics to identify indicators of instability and rupture risk [4][32]. In parallel, radiomic investigations have allowed to extract hundreds of quantitative features from images, expanding prediction and tailored treatment possibilities [33]. On the other hand, advances in biomechanics have incorporated computational models that consider wall stress and its resistance, offering another histopathological approach for risk stratification [31]. Finally, the integration of omic approaches, like genomic and transcriptomic studies, have provided new insights into the biology of AAA, although linking these molecular findings to structural and mechanical disease aspects remains a challenge [4][33].

Together, these areas of research reinforce multidisciplinary perspective on AAA, highlighting the need to integrate morphological, biomechanical, and molecular information to find new biomarkers that allow to advance toward more personalized and precise patient care.

3. STATE OF THE ART

AAA, which is usually asymptomatic, affects primarily to men older than 60 years and it is one of the most common sudden death causes for the elderly [34]. The fact of generally being asymptomatic, causes that the detection is usually an incidental finding when performing an ultrasonography, CT, or MRI for other purposes [34]. The rupture risk increases exponentially with the diameter, expansion rate, uncontrolled hypertension, and active smoking [1].

Although surgical techniques have improved significantly in recent years, there is still no pharmacological therapy that has convincingly demonstrated efficacy in slowing AAA growth in randomized controlled trials. A wide range of drugs has been tested, including antibiotics, blood pressure lowering therapies like fenofibrate or PSCK9 inhibitors [1]. However, none of these approaches have shown consistent benefit. Some observational studies suggest that metformin and ACE inhibitors might be associated with slower aneurysm growth or reduced rupture risk, but this evidence remains preliminary and is currently under investigation in clinical trials [1].

Traditionally, the clinical management of AAA has relied on the transversal maximum diameter as the main indicator to decide whether there should be a surgical intervention or not and which would be the most precise for the situation. Although transversal maximum diameter is a known risk factor for AAA growth and rupture risks, diverse studies have shown an interindividual variability, which limits the predictive capacity as a unique clinical indicator [30]. This is why, in the last decades, new trends based on morphological, biomechanical or radiomic characteristics have become more popular [33].

In this context, the development of automatic algorithms that enable to extract in a precise and reproducible these properties from aorta segmentations have emerged as a promising area of research. These methods can contribute to improve clinical practice and progress in translational vascular research.

3.1 Morphological Studies of Abdominal Aortic Aneurysm (AAA)

3.1.1 Centerline Extraction and Tortuosity

Centerline analysis is a fundamental tool in the morphological evaluation of AAA. It allows to obtain quick and reproducible measurements of diameters and lengths along the vessel, which provides essential information for diagnostics, monitoring, and preoperative planning. Compared with manual multiplanar reformation (MPR), centerline-based measurements offer higher precision in tortuous or complex vascular anatomies, provided that it follows the real aorta trajectory [35].

Zhang et al. [32] proposed a robust semiautomatic method to detect the centerline of the aortic lumen in AAA by using AdaBoost online classifiers, without needing previous segmentation (*Figure 6*). The method proved a high precision when it was tested in 60 datasets (30 ruptured and 30 unruptured AAAs). Their results revealed that tortuosity was significantly higher in ruptured aneurysms, suggesting that it may be useful as a geometrical biomarker to assess rupture risk [32]. On the other hand, other authors, like Fillinger et al., reported an opposite tendency (lower tortuosity in ruptured aneurysms), this discrepancy is probably due to the use of bidimensional methods that underestimate the real three-dimensional lumen geometry [32].
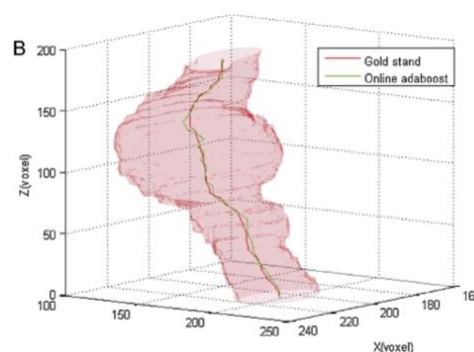
Figure 6: Comparison of classical centerline extraction methods vs. AdaBoost online classifiers [32].

Other studies that compare the anatomy of ruptured and intact aneurysms have shown that the ruptured AAAs tend to have shorter necks and larger diameters [36]. These anatomical factors are relevant for rupture risk, but also for determining the feasibility and safety of EVAR procedures.

Additionally, Bodur et al. [37] proposed a semi-automatic method for extracting the aortic lumen centerline and segmenting the outer vessel wall, including intraluminal thrombus, using a modified isoperimetric segmentation algorithm, which enables full 3D reconstruction. This approach not only facilitates automatic diameter calculation from orthogonal cross-sections, but also other measures such as transversal areas, or shape descriptors.

3.1.2 3D Morphological Indices and Rupture Risk Prediction

In recent years, 3D segmentation methods have allowed to extract complex morphological descriptors from angio-CT images. Tang et al. [38] developed a wide case-control study comparing ruptured and asymptomatic aneurysms, and found that several 3D geometrical indices, such as sac height, wall surface area, thrombus volume, bulge location, and mean averaged area curvature, were significantly associated with the risk of rupture, even after adjusting for maximum diameter and gender.

These insights are reinforced by cerebral aneurysms studies, where automatic feature extraction from radiological images has proved that shape irregularity is a better rupture predictor than size [39][40][41]. For example, parameters like flatness, superficial area, sphericity, or spherical disproportion, have been all identified as key features to distinguish stable from unstable aneurysms (*Figure 7*) [39]. Although the anatomical context is different, the conceptual parallels suggests that similar morphological irregularities may also be valuable for AAA risk evaluation.
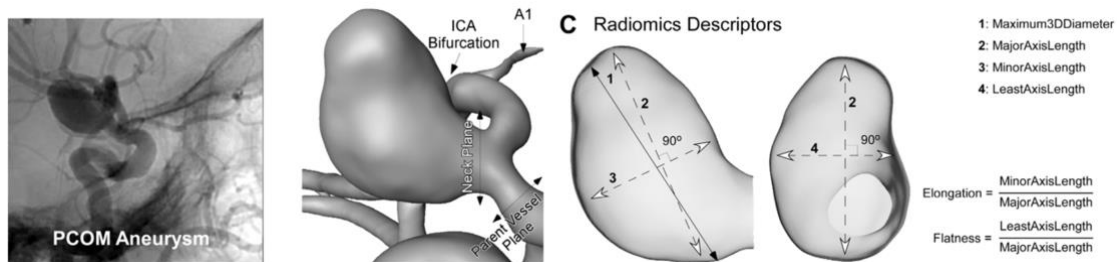
Figure 7: Shape descriptors of cerebral aneurysms [41].

Also, anatomical configurations like conical or barrel-shaped necks, high angulation, and thrombus-laden walls have been associated with high increased risk of endoleaks and graft migration, according to interventional studies [42].

In addition, Wadgonkar et al. [43] highlight the utility of multiplanar reconstruction (MPR) and semiautomatic tools to obtain precise measurements that are orthogonal to the centerline, which significantly reduces the interobserver variability. They also describe key indicators of instability, such as the crescent sign (hyperattenuating intramural hemorrhage), the draped aorta sign (deformation of the aneurysm sac over the vertebrae), mural thrombus lysis, and focal discontinuity of intimal calcifications [43]. These findings together with the observation of decreasing thrombus volume and rapid lumen expansion, reinforce the idea that rupture risk prediction should be based on a combined approach involving both morphological metrics and visual radiological patterns.

3.1.3 Calcification and AAA Risk

Vascular calcification is a well-established cardiovascular risk factor, and its role in rupture risk and aortic aneurysm progression has been of interest in recent studies.

A study performed by Bujis et al. [44] found that calcification was significantly higher in patients with symptomatic or ruptured AAA compared to those undergoing elective repair. Specifically, both larger diameters and higher calcification score were independently associated with rupture or symptoms, supporting the hypothesis that said that calcification can contribute to structural degradation of the aortic wall [44].

O'Leary et al. [45] provided mechanical insights by performing mechanical tests in AAA tissue samples, comparing fibrous regions to partially calcified areas. Their results showed that rupture frequently occurred at the interface between calcifications and the surrounding fibrous matrix [45].

In contrast, Klopf et al. [46] found an inverse relationship between calcification volume and aneurysm growth. Increased calcification volumes were associated with a slower aneurysm expansion, suggesting a possible stabilizing effect, as represented in *Figure 8*. This finding highlights the complex and potentially dual function of calcifications: while it can weaken locally the aortic wall, it could also limit the global aneurysm expansion [46].
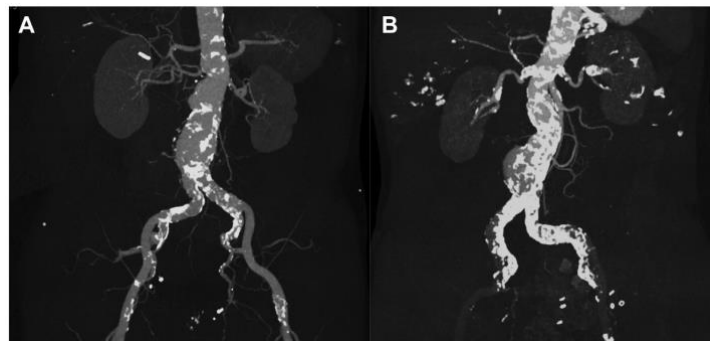
Figure 8: Differences of calcification patterns in patients with AAA. CT showing an AAA with little vessel wall calcification and increased progression (A) compared with an AAA with a higher calcification but decreased AAA growth rate (B) [46].

In summary, calcification within AAA wall is increasingly recognized as a complex factor in the aneurysm physiopathology. Although it seems to contribute to local mechanical weakening of the wall, some data suggests that it could have a stabilizing effect limiting the aneurysm growth. Understanding these dual effects is key to improve risk stratification and decision making in AAA.

3.1.4 Morphological Key Parameters in AAA

In summary, morphological characterization of AAA has evolved thanks to 3D segmentation methods and advanced analysis, which has enabled to identify key parameters for risk stratification and treatment planning. As shown in the study performed by Rezaeitaleshmahalleh et al. [47], indexes derived from the centerline, like tortuosity, and 3D geometrical measures, such as aneurysm volume and total surface, stand out for their relevance ($p < 0.05$) and have shown significative differences between rapid-growth and slow-growth aneurysms. Particularly, variables like lumen tortuosity ($p = 0.01$), lumen and thrombus volume ($p = 0.04$), and the maximum/minimum radius ratio ($p = 0.02$), are especially relevant. These measurements offer a more complete and

complementary view of the classical criteria based on maximum diameter, helping to better understand the differences in morphology and improve rupture risk prediction and stratification.

3.2 Radiomic Techniques on AAA Evaluation

Radiomics is an emerging field that allows to extract a large number of quantitative features from medical images, converting the visual information into numerical data that can better describe morphology and texture with high precision. This technique offers new opportunities for personalized risk stratification and AAA evolution, complementing the classical anatomical measures based only on the diameter [26].

3.2.1 Biological Interpretation of Radiomic Features

Although radiomics offers a high amount of quantitative data, its clinical acceptance requires to understand how these features are related with biology. Tomaszewski and Gillies [26] highlight that the radiomic features derived from matrices such as GLCM-derived entropy, run-length emphasis (GLRLM), size zone variability (GLSZM) and wavelet transforms usually reflect histopathological key aspects related to tissue microarchitecture, including fibrosis, necrosis, or inflammatory infiltration. High entropy and low run-length emphasis, for example, can indicate more complex and disordered tissue, potentially correlating with areas of active aneurysm remodeling and inflammation.

3.2.2 Radiomics of Perivascular Adipose Tissue (PVAT)

The perivascular adipose tissue (PVAT) surrounding the aorta is now recognized as an endocrine organ capable of secreting various adipokines, cytokines, and growth factors that influence vascular biology. In AAA, a raise in PVAT attenuation has been associated with aneurysm growth and the infiltration of inflammatory cells [48].

Lv et al. [48] studied the radiomic characteristics of PVAT in patients who underwent EVAR and found that growing aneurysms showed a higher surface area-to-volume ratio (0.70 vs 0.63, p=0.04) and greater textural heterogeneity compared to non-growing aneurysms. Texture features, including those derived from grey-level co-occurrence matrix (GLCM), grey-level dependence matrix (GLDM), and grey-level run-length matrix (GLRLM), also differed significantly (p<0.05). For example, the dependence variance and long run emphasis, were lower in growing AAAs, indicating a more uniform texture, while the run-length non-uniformity was higher reflecting greater heterogeneity in PVAT structures. These findings suggest that textural features of PVAT may reflect underlaying inflammatory or remodeling processes that promote AAA growth [48].
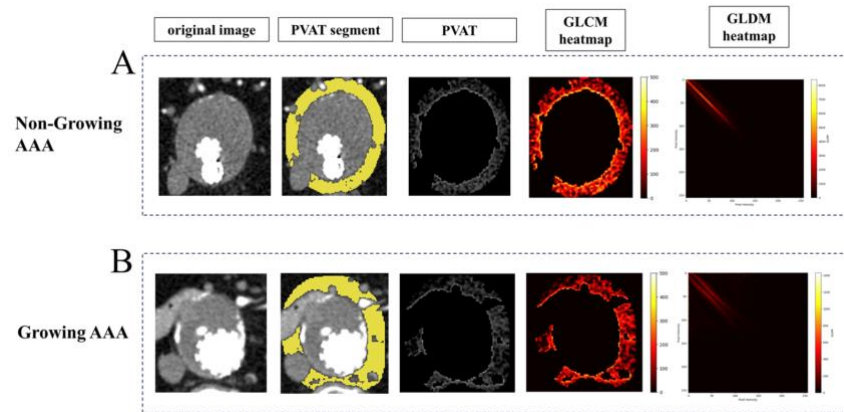
Figure 9: Visualization of texture features in PVAT. The top row represents a non-growing AAA (A) while (B) represents a growing AAA. The 1st image of both shows the arterial phase enhanced CT slice. The 2nd represents the manual segmentation of PVAT. The 3rd depicts the extracted PVAT. The 4th and 5th images display the heatmaps of the GLCM and GLDM respectively [48].

3.2.3 Radiomic Analysis of Intraluminal Thrombus (ILT)

The ILT has been a focus in recent studies due to its role in AAA rupture risk. Rezaeitaleshmahalleh et al. [47] applied an automatic ILT radiomic analysis, proving that the incorporation of texture characteristics of the ILT significantly improved the prediction of AAA growth. Among the most relevant features are included geometrical metrics and composition parameters of the thrombus [47]. Wang et al. also reported improvements in prediction when incorporating radiomic information of the ILT. Key radiomic features identified include wavelet-transformed energy metrics and texture features capturing ILT structural heterogeneity, which may reflect differences in thrombus stability and remodeling and identify more precisely the aneurysms with rapid growth [49].

3.2.4 Challenges and Future Directions

These results consolidate the idea that radiomic analysis of specific regions like ILT or aortic wall, provide precise complementary information and highlights the need to keep progressing in the validation of these models. Despite all the advancements, radiomics faces several challenges: the reproducibility of features depends on image and segmentation quality, acquisition parameters and analysis standardization [29]. Moreover, the biological meaning of many radiomic features is still unclear in AAA, which highlights the need for wider prospective studies and multimodal integration (clinical, radiomics, biomechanics) to consolidate its use in clinical practice.

3.3 Automatic Segmentation Algorithms

Abdominal aortic aneurysm segmentation from medical images is essential for a precise evaluation and for interventional planning. Traditionally, this task has relied on manual delineation by radiologists, a long process and susceptible to variability. This is why, in the last years, multiple automatic and semi-automatic methods have been developed with the aim of reducing time and increase segmentation reproducibility, providing benefits in clinical practice and research.

3.3.1 Approaches Using MRI and Traditional Image Processing Methods

One of these methodologies is presented by Martínez-Muñoz et al. [50], who developed an automatic algorithm to segment AAA in RM images: first, the aortic lumen was segmented using a diffuse clustering algorithm (SFCM) and morphological operations; then, the aortic wall and

thrombus were segmented with graph cuts and using the lumen segmentation as an automatic initializer. This approach allowed to obtain satisfactory results in a mean time lower than 3 seconds, with a superposition of 79% with respect to the manual segmentation performed by an expert.
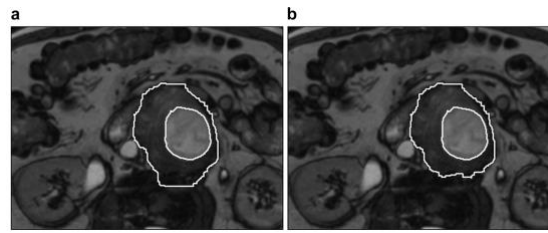
Figure 10: Example of aortic segmentation with an automatic method compared with an expert-validated segmentation. (a) Segmentation obtained automatically using Martínez-Muñoz et al. method and (b) segmentation by the expert [50].

3.3.2 Automated Methods for CT Images and Border Propagation

Lareyre et al. developed a completely automatic software that combines border propagation and morphological techniques to segment the aortic lumen and thrombus in angio-CT images. This system demonstrated precision to segment AAA and allowed to visualize 2D and 3D reconstructions, facilitating the detailed analysis of aneurismatic morphology [51].

3.3.3 Approaches Based on Deep Learning

More recently, Abdolmanafi et al. proposed a fully automated segmentation model based on deep learning to segment the aorta and the associated structures (lumen, wall, thrombus, and calcifications) using convolutional deep neural networks (CNNs). Their model, which uses an encoder-decoder architecture based on ResNet, showed an excellent performance comparable to the one performed manually by experts [52].

On the other hand, Mu et al. presented the CACU-Net, a two-stage 3D deep learning architecture with dilated convolutions and anisotropic context module for fully automatic lumen and thrombus segmentation in CT angiography data. This model significantly outperformed other methods (such as 3D U-Net or Graph Cuts) [53].

Caradu et al. evaluated a fully automated segmentation software (PRAEVAorta) comparing it with manual segmentations corrected by experts (*Figure 11*). Their analysis showed excellent correlation, reducing the segmentation time from 5-80 minutes manually to 27seconds-4minutes automatically [54].
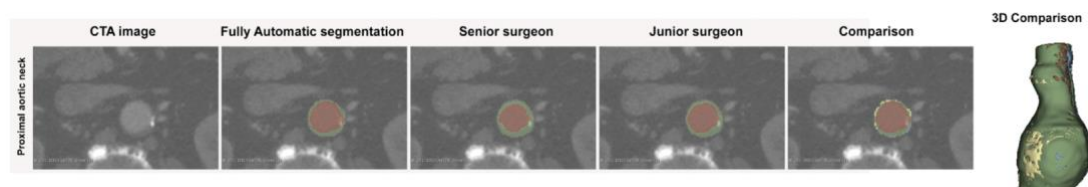
Figure 11: PRAEVAorta segmentation results. Representative images of the segmentation of the aortic lumen (red) and the intraluminal thrombus (green). A comparison of the results obtained with the fully automatic segmentation and the manually corrected segmentation by surgeons are also displayed, showing the mismatched regions in yellow [54].

Finally, Sieren et al. trained a model based on a 3D U-Net to completely segment the aorta (lumen, wall, thrombus, calcifications) in angiographic CTs. Their method accomplished a mean Dice of

0.95, validating the precision of an automated approach compared to manual expert segmentation [55].

These studies prove the importance and evolution of automatic segmentation methods in AAA. Most studies and implementations show evidence that automatic segmentation not only can be used as a tool to reduce time and workload for specialists, but also to standardize results and improve diagnostic precision and interventional planning.

3.4 Biomechanical Assessments

Biomechanical evaluation of AAA offers a promising alternative to improve prediction of rupture risk and intervention planning, complementing the diameter-based evaluation. These methods use computational models that consider physical and geometrical properties of the aneurysm to estimate parameters like peak wall stress (PWS), peak wall rupture index (PWRI) or the aneurysm biomechanical ratio (ABR).

A study by Doyle et al. demonstrated that ABR, defined as the dimensionless ratio of local wall stress to wall strength, is an independent predictor of events related with the aneurysm (rupture or repair) [15]. The ABR calculation applies physiological pressures to 3D aneurysm reconstructions to simulate hemodynamic conditions. The study revealed that patients with a higher ABR presented a higher rupture probability of the aneurysm, highlighting the potential of this index for risk stratification and clinical planning.

On the other hand, Singh et al. investigated the role of PWS and PWRI in predicting aneurysm-related events in patients with small AAAs. Their finite element analysis (FEA) revealed that while both were related with a higher rupture risk, only PWRI significantly improved the risk classification beyond maximum diameter [31].

As a notable example for biomechanical analysis, the BioPARR software has been specifically developed to estimate the Rupture Potential Index (RPI) from CT or MRI images. This software combines semi-automatic segmentation and FEA simulations in a fully automatized workflow, to estimate wall stress and rupture potential, removing the need for detailed knowledge of patient-specific material properties and making biomechanical risk assessment more accessible for clinical practice [56].
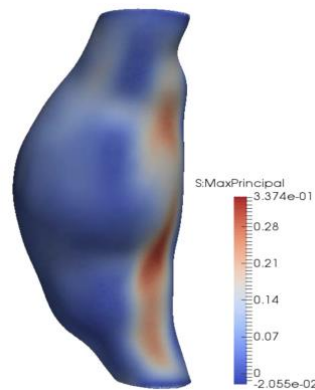
Figure 12: Example of stress computation results by BioPARR. The maximum principal stress [MPa] is computed at each node of the finite element mesh [56].

The incorporation of softwares like BioPARR in research and clinical practice that can calculate parameters like ABR or PWRI could allow for a more specified risk stratification and improve the results in patients with AAA. However, additional studies and validation in independent cohorts are still necessary to consolidate these tools as an integral part of clinical practice.

Although this project initially considered the extraction of biomechanical features using tools like BioPARR, the final implementation focused exclusively on morphological and radiomic features due to time constraints and the need for manual segmentations. Nevertheless, biomechanical analysis is included in the state of the art as a promising complementary approach, potentially valuable in future extensions of the pipeline.

4. STATE OF THE SITUATION

4.1 Clinical Need and Current Limitations

Currently, the main indicator to decide AAA management is the maximum transversal diameter, measured manually by radiologists using CT or US images. However, this classical measurement presents limitations: it is highly operator-dependent, subject to interobserver variability, and it also fails to capture the full complexity of the aneurysm morphology. Defining the size of the AAA only with the maximum diameter presents a high irreducible error, as other important features such as ILT or calcifications are not considered, even though they play a crucial role in aneurysm behavior. As a result, some aneurysms rupture before reaching the surgical threshold, while up to half of those undergoing repair would never have ruptured if left untreated [8].

Consequently, using diameter alone may not take into account relevant features that can influence in the aneurysm progression or instability, highlighting a medical need to incorporate complementary features into AAA evaluation.

4.2 The Importance of Automatic Feature Extraction

Considering these limitations, the need of developing robust and automatic methods to extract morphological and radiomic features directly from medical images appears. These algorithms have the potential to offer reproducibility, precision, and independence from operator bias, which are

essential for both research and clinical practice and research. Furthermore, they allow to process large volumes of data in a rapid and standardized way, facilitating the development of large-scale studies and translational applications. Such algorithms could also lay the foundation for future integration with omics data.

4.3 Project Motivation and Clinical Impact

Recent studies have highlighted features beyond diameter that could serve as clinically relevant biomarkers to assess AAA behavior. Importantly, these morphological and radiomic characteristics might better correlate with the biological processes revealed by omics studies, like transcriptomic or miRNA signatures, which often show little relationship with diameter alone. Incorporating such diverse parameters offers a more comprehensive and individualized characterization of aneurysms, capturing subtle changes that diameter-based evaluations may miss (for instance, growth in volume or complex remodeling that does not translate to diameter increases). This motivation arises from the observation that some genes or RNA molecules identified in omics studies may not correlate with maximum diameter but could relate to other morphological or radiomic features. The current approach of using only maximum diameter as a ground truth, measured visually and manually by radiologists, is insufficient for these broader goals. Developing an automatic, precise, and reproducible algorithm for extracting these complementary features is therefore a necessary step.

Furthermore, since AAA growth can sometimes occur in ways that do not translate into diameter changes, such as longitudinal expansion or remodeling, diameter alone may miss important disease processes. Developing such an algorithm could not only enhance basic research in omics studies, but also lay a groundwork for clinical applications, enabling more personalized follow-up and treatment planning for AAA patients.

5. MARKET ANALYSIS

The development and implementation of automatic feature extraction algorithms in the field of AAA diagnosis and treatment planning represents a rapidly growing area with significant clinical and research interest. In this section, we present a market analysis focusing on the current landscape, main players, and trends shaping the adoption and evolution of these technologies.

5.1 Market Overview: Automatic Feature Extraction Algorithms

The extraction of morphological and radiomic features from medical images has acquired an increasing relevance in the field of vascular and cardiovascular imaging. Traditionally, 3D Slicer has been a key tool in research environments, allowing for the manual or semiautomatic extraction of basic geometrical descriptors such as centerline, diameters, or volumes [57]. However, since it does not have clinical approval, its application is limited to research. Additionally, it does not allow for the extraction of complex geometrical or radiomic features.

In clinical practice, Mimics offers a software platform with CE marking, which enables the extraction of semiautomatic features [58], allowing to extract more complex features than 3D Slicer. However, it is still semiautomatic and therefore operator dependent, especially for complex features.

To overcome these limitations, the market is being oriented towards fully automatic methods that integrate segmentation with automatic feature extraction modules. Advances in deep learning approaches, with models like U-Net and 3D U-Net, allow to automatically extract morphological metrics [53][55]. At the same time, tools like PyRadiomics facilitate the extraction of radiomic characteristics [59], while platforms like BioPARR incorporate biomechanical analysis [56].

Patent literature also reflects this evolution. For example, US8781193B2 describes automatic systems for blood vessel quantitative analysis [60], CN104619244B proposes non-invasive methods with ultrasounds and radiofrequency [61], and WO2010121146A2 uses three-dimensional analysis based on vascular morphology [62]. Furthermore, open-source tools such as AneuPy allow to generate AAA geometries to be used for simulation and algorithm validation [63].

However, any patented product or scientific article has been found that, in the context of AAA, integrates in a fully automatic single flux the extraction of both simple and complex geometrical and radiomic features from the original image and segmentation. This places the algorithm proposed in this project as an innovative proposal and with a high potential in clinical and research applications.

5.2 Target Market

The development of completely automatic feature extraction algorithms applied to AAA images targets a specific and growing market within the medical imaging and cardiovascular disease management sectors. This market includes several key players:

- **Clinical research institutions and academic hospitals:** Research groups focused on personalized medicine and integration of new biomarkers based in imaging to predict growing or rupture risk of AAA.
- **Healthcare providers and hospitals:** Medical centers and vascular surgery services which require precise morphological analysis for diagnostic, evolution assessment and treatment planification of AAA.
- **Medical device manufacturers:** Companies that develop or integrate imaging diagnostic tools, like Philips Healthcare or Siemens Healthineers, are increasingly interested in incorporating automated and advanced solutions.
- **Startups and software companies:** Smaller companies, specialized in radiomic and imaging analysis using AI, such as QUIBIM or Persomic, that could be interested in licensing or integrating new algorithms into their platforms.
- **Pharmaceutical companies:** Firms aiming to evaluate the effectiveness of their treatments through advanced imaging biomarkers may find value in automated morphological and radiomic analysis tools.
- **Regulatory bodies and insurance companies:** As automatic algorithms become more clinically validated and integrated, these stakeholders may also be relevant for ensuring compliance with data protection and clinical safety standards.

By offering a fully automated feature extraction algorithm, including morphological and biomechanical metrics, the algorithm developed in this project answers the clinical need of a more precise and reproducible AAA characterization.

5.3 Future Perspectives of the Market

The market for feature extraction algorithms in the context of AAA presents a promising future, driven by several key trends. On the one hand, the advancement of personalized medicine and the need of precise and reproducible imaging biomarkers are increasing the demand for automated solutions that go beyond the limitations of manual measurements.

In addition, the progressive integration of artificial intelligence into clinical workflows supports the adoption of these algorithms, especially if they are compatible with hospital platforms. In parallel, the regulatory landscape is evolving towards clinical certification of these tools and the access to multicentric databases will allow to validate its robustness in real populations.

Overall, a sustained growth is expected in this market, and solutions like the one proposed in this project, which integrate morphology and radiomics, are well positioned to meet this demand.

6. CONCEPT ENGINEERING

This project aims to develop a computational pipeline to extract morphological and geometrical features from CT images of patients diagnosed with AAA. Even though maximum diameter is currently the main clinical indicator used to monitor the aneurysm progression and determine the need for surgical intervention, this metric by itself does not capture the full morphological complexity of the aneurysm. The objective of this project is to obtain complementary descriptors to improve characterization and evolution follow-up of the AAA.

The study is based in a set of patients diagnosed with AAA. The database consists of contrast-enhanced CT of these patients which then, during the project, will be segmented into key structures: abdominal aorta, renal arteries, superior mesenteric artery, and iliac bifurcations, all of them separated into lumen, intraluminal thrombus, wall, and calcifications. From these segmentations, a structured and automated computational pipeline has been developed which processes every image, identifies anatomical points of reference, and calculates different geometric and radiomic features of clinical interest.
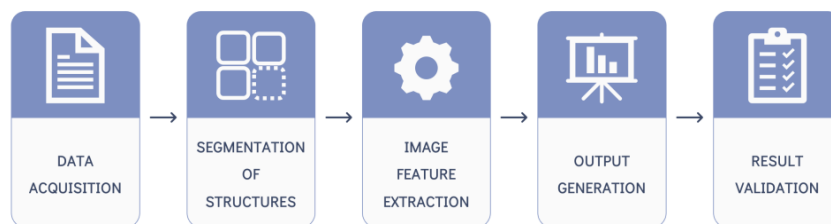
Figure 13: Main stages of the project workflow.

As it can be seen in *Figure 13*, previously shown in the methodology section, the pipeline is organized in five main stages that illustrate the conceptual structure of the engineering design:

1. **Data acquisition**, which includes CT image retrieval and patient selection.
2. **Preprocessing and segmentation**, where anatomical structures are segmented, and binary masks are prepared for analysis.

3. **Feature extraction**, in which geometric descriptors are computed from the segmented volumes.

4. **Output generation**, where numerical results are compiled into summary tables and visual plots are produced.

5. **Result validation**, which includes comparison and consistency checks using available patient-specific clinical information.

6.1 Data Acquisition

The data acquisition stage involves obtaining medical imaging data of patients diagnosed with AAA. CT scans may be acquired for various reasons, either incidentally while investigating other conditions, or as part of regular follow-up for known aneurysms, and are stored in the hospital's clinical imaging system. Once the images are retrieved from clinical repositories, they are converted from their original DICOM format to a more manageable format (such as NIfTI) to facilitate storage, anonymization, and subsequent volumetric processing. For optimal data management and reproducibility, images are typically organized in a hierarchical folder structure by patient and acquisition date, ensuring a systematic and automated approach to data access in later pipeline stages.

6.2 Preprocessing and Segmentation

In this stage of the pipeline, the anatomical segmentation of the relevant structures from the CT images is performed. Since the original images come from an existing database, no normalization nor resampling is applied; these operations, in case they are needed, are applied in posterior feature extraction steps. A key aspect of this stage is to define a standardized and reproducible pipeline so that any user can segment the images in a consistent and uniform way, minimizing variability between operators.

The main goal of the segmentation process is to isolate the different anatomical regions that constitute the abdominal aorta and its ramifications. Specifically, the following structures are segmented: abdominal aorta (including both supra and infra-renal sections), left and right renal arteries, superior mesenteric artery, celiac trunk and left and right iliac arteries up to their bifurcations. Moreover, each of these segments is then separated into its internal components: lumen, intraluminal thrombus (ILT), aortic wall and calcifications. It is important to note that both thrombus and calcifications are included also in the wall structure.

Some tools available for segmentation are for example Mimics, which is a paid and closed-source software, or 3D Slicer, which is open-source.

All segmentations correspond to a same patient and are stored in a single *.nrrd* file, which includes multiple labels organized through a system of labels and layers. Each label corresponds to a specific anatomical structure and follows a standardized nomenclature which is constant in all patients (for example, *Lumen_IRA* for the left renal artery lumen, or *Wall_CT* for the wall of the celiac trunk).

Once this segmentation process is finished, the resulting files are integrated directly on the next pipeline stage, destined to automatic feature extraction of morphological, geometrical and radiomic features.

6.3 Feature Extraction

Once all segmented masks are obtained, the next step of the pipeline consists of the automated extraction of geometric, morphologic and radiomic features for each individual study. This stage focuses on the main aorta, considering both its infra- and supra-renal section, and analyzing separately the four anatomical structures: lumen, ILT, aortic wall and calcifications.

Below, *Table 1* summarizes the main groups of features identified from the state-of-the-art literature, specifically those that have demonstrated significant associations in previous studies and will be used in this analysis.

These feature groups include shape and spatial configuration, cross-sectional and volumetric parameters, and radiomic features that capture textural and intensity patterns.

Feature Group	Examples	Meaning	Potential Biological Relevance
Shape & Spatial Configuration	Centerline, tortuosity, curvature	Reflect overall vessel path, focal deformation, and remodeling.	Associated with aneurysmal remodeling, rupture risk and local wall stresses.
Cross-Sectional Measurements	Cross-sectional area, diameter, circularity	Quantify size and shape of vessel cross-sections at various points	Inform about local expansion and structural irregularities in 2D slices.
Volume	Lumen, ILT, Calcifications volume, volume ratios	Provide 3D quantification of structures and their relative occupation	Reflect aneurysm progression, remodeling dynamics, and hemodynamic changes.
Radiomic features	Entropy, skewness, kurtosis	Capture intensity distribution and texture complexity	Potentially related to inflammation, thrombus, composition, tissue remodeling

Table 1: Main feature groups of interest to be extracted through the automated pipeline.

All these calculations are performed individually for each study (per patient and date), without establishing any temporal comparation between acquisitions. The results generated in this stage are structured value tables, which will be compiled and visualized in the next stage of the pipeline.

Several tools are available for feature extraction, many of which are open source and implemented in Python. Examples include PyRadiomics for radiomics analysis, PyVista for 3D mesh operations, scikit-image for image processing and SciPy for geometric computations.

6.4 Visual Representation of the Features

This stage of the pipeline consists of compiling and organizing the numerical results generated in the feature extraction process. To ensure that the information is accessible, clinically interpretable, and ready for further analysis, three main types of output tables are produced:

- **Detailed feature tables** with all measured values for both acquisitions, to generate a large dataset for further research studies.
- **Key parameter changes tables** highlighting percentage changes between both acquisitions.
- **Centerline evolution tables** showing how features vary along the aorta.

Additionally, a medical report for each subject, synthesizing the quantitative results and accompanied with visual plots, will be generated for clinical interpretation and expert validation. This report can be used for a single acquisition visualization, or to compare different acquisitions of the same patient.

6.5 Result Validation and Analysis

The final stage of the pipeline focuses on the validation of the extracted data and the analysis of the generated results, with the aim of ensuring its clinical reliability and research relevance. Typical validation mechanisms usually include comparison of obtained measures with reference values, reproducibility evaluation and performing quality controls to verify data coherence. Moreover, descriptive, and exploratory analysis is carried out to identify patterns and tendencies in morphological and radiomic features between patients or between acquisitions, which allows to obtain information of the aneurysm's structural evolution. This validation and analysis stage is essential to confirm that the automatic pipeline offers precise and significative results from a clinical point of view, laying the groundwork for future applications in both clinical practice and research.

7. DETAILED ENGINEERING

7.1 Data Acquisition

The data used in this project is obtained from the Triple A Barcelona Study (TABS), a clinical cohort with 488 patients diagnosed with AAA and having multiple CT images obtained in different temporal moments. The original CT images were obtained through the Agfa Healthcare Enterprise Imaging system, the platform used to access and visualize DICOM data stored in the hospital servers.

For this proof of concept, a sample of 10 subjects was selected. The selection of patients from the TABS cohort was carried out manually and based on the following inclusion criteria:

- Availability of two CT scans separated by approximately 1 to 2 years.
- Adequate image quality for segmentation purposes.
- A sample distribution that included patients with both slow and fast aneurysm growth.

All the patients selected were men between the ages of 58 and 83 years. The classification between patients with rapid or slow growth was performed by calculating the growth rate in mm/year using the maximum aortic diameter values reported in the medical reports. The ten patients with the most contrasting growth rates were selected: the five with the fastest growth and the five with the slowest growth. In *Figure 14*, a representation of this process can be seen. This was performed with the aim to explore differences in growing patterns, basing this information in the change observed in the maximum diameter in both studies, information that was observed by expert radiologists and stored in the medical report.
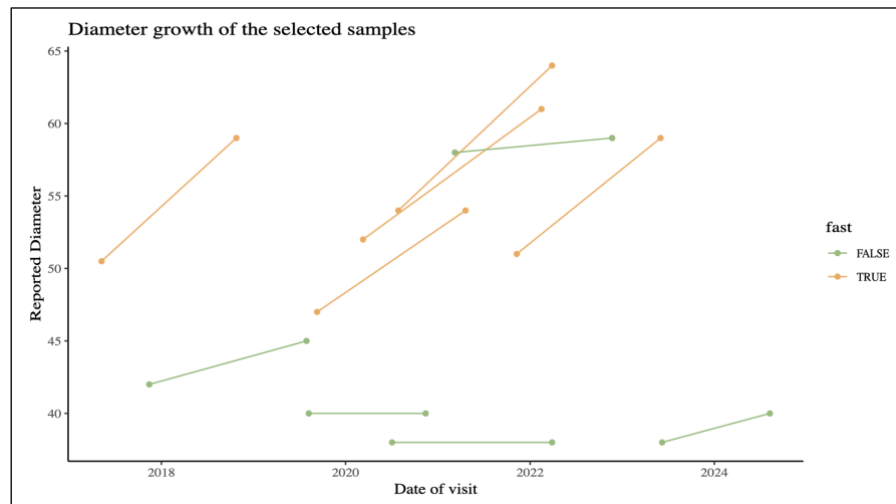
Figure 14: Plot representing patient's aneurysm growth rate classification. Orange represents fast growth and green slow growth.

The DICOM images were converted to NIfTI format using 3D slicer, and they were locally organized with a hierarchical folder structure by patient and acquisition date. A rout example would be:

```
/Patients/SP0006/2018-10-25/SP0006_2018_10_25.nii.gz
```

Figure 15: Folder structure to store segmentations.

Each date folder will include both the image in NIfTI format and its corresponding segmentation in NRRD format when it is created in further steps.

7.2 Preprocessing and Segmentation

The segmentation process was performed manually using 3D slicer platform, with the support of semiautomatic tools available in the program. To guarantee consistency and reproducibility across all patients, a standardized segmentation process was defined, which was validated by the personnel of Dimension Lab at Hospital de Sant Pau. Although the lab did not verify each segmentation individually, the methodology was reviewed and approved to guarantee clinical coherence.

Each patient's segmentation was stored in a single *.nrrd* file, which contains all structures as labeled segments. These are distributed across different layers depending on whether there is overlap between them, and each segment is assigned both, a numeric label, and a custom name (*Lumen_IRA* or *Wall_CT for example*). The spatial metadata within the file is preserved in the *header* to enable accurate downstream geometric and radiomic calculations.

Segmentation workflow overview:

▪ **Lumen:** Segmented using the *Fast-Marching* algorithm (*SegmentEditorExtraEffects* extension). An initial seed was defined with the *Paint* tool, and volume thresholds were adjusted to avoid inclusion of other anatomical structures. Then it defines the region by moving faster in similar-intensity regions and slower at edges, defining the fastest path. Manual corrections were made when necessary (*Figure 16A)*. On the other hand, the *Fast-Marching* algorithm did not work well for images with low intraarterial contrast, so in this case, *Threshold* tool was used and manually adjusted to segment the lumen.

26

- **Thrombus (ILT):** Segmented with the *Grow from Seeds* method, which expands labeled regions from seed points by assigning each voxel to the closest seed, using image intensity and spatial distance. Seeds for both thrombus and background were manually painted in multiple slices. Seed locality was maximized to reduce oversegmentation, and further seeds were added to correct misclassified areas (*Figure 16B*).

- **Wall:** Derived by combining the lumen and thrombus masks. The *Margin* tool was used to grow the lumen segment by 2mm, and logical operations (copy, add, hollow) were applied to generate a medial-surface shell of 1.5mm representing aortic wall (*Figure 16C*).

- **Calcifications:** Identified using the *Threshold* tool after contrast adjustment. A mask expansion was performed to isolate the calcifications from bone structures, and logical intersections were applied to constrain them within the vessel region (*Figure 16D*).

- **Structure refinement:** Logical subtractions were applied to remove overlaps. The wall segment was redefined by adding both the thrombus and calcifications.

- **Region of interest delimitation:** Markers were used to trim all vascular segments to a standardized length within 3 cm from each branch origin (*Figure 17*).

- **Vessel branch separation:** The full aortic segmentation was divided into its constituent branches (suprarenal and infrarenal aorta, renal arteries, superior mesenteric artery, celiac trunk, and iliac arteries), using manual cuts and logical operations to maintain internal structure consistency.
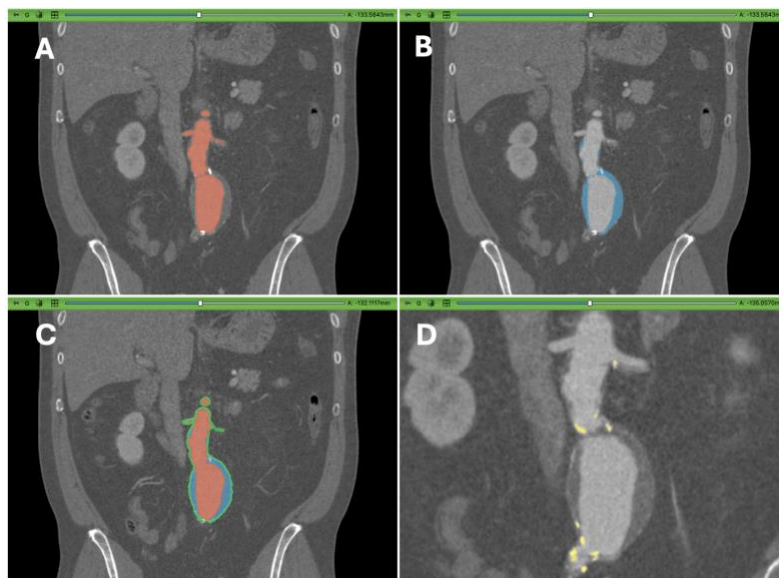
Figure 16: Segmentation workflow representation. Segmented following the order: lumen (A), ILT(B), aortic wall (C) and calcifications (D).
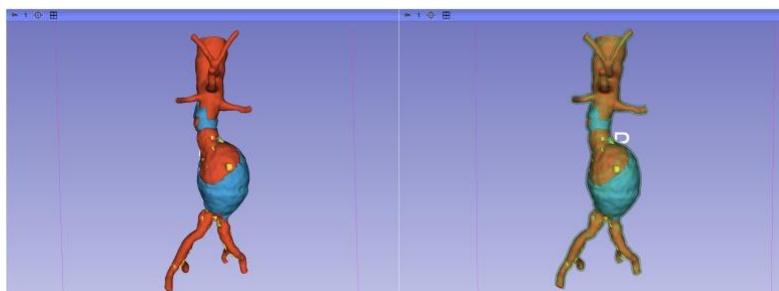
Figure 17: Final segmented aorta with the ROI delimited within 3cm from each branch.

Each branch preserves the four main internal structures (lumen, thrombus, wall, calcifications), unless one or more are not present. This segmentation format ensures that all elements are structurally consistent and ready to be processed automatically in the next stage of the pipeline.

7.3 Feature Extraction

In this section, a comprehensive and structured description of the steps and methods used for extracting morphological, geometrical and radiomic features from the segmented masks of each patient is provided. This automated process is implemented in the *process_patient.py* script, which uses various functions defined in *utils.py* to perform precise calculations and generate clinical insights. The following blocks detail each step.

All the code used in this project is available in a public GitHub repository[2], specifically in the *pipeline* folder, which contains the file *utils.py* (defined functions), *process_patient.py* (feature extraction from a single image acquisition) and *run_single_patient.py* (full and automatic processing of two acquisitions for one patient and generation of visual outputs).

7.3.1 Centerline and Global Geometry

The first step in feature extraction involves obtaining a continuous and smooth centerline that represents the path of the aorta along its length. To achieve this, a combined mask of lumen and ILT (*Lumen_Thrombus_A*) is smoothed with a Gaussian filter (*gaussian_filter*) and skeletonized in 3D (*skeletonize_3d*) obtaining the central voxels of the segment. The function *get_centerline()* then extracts the main path using a minimum spanning tree (*minimum_spanning_tree*) and smooths it through spline interpolation. Then, using the *header* spatial and origin information, the centerline coordinates are converted to world coordinates in millimeters, using the *voxel_to_world_coords()* function, which implements the following expression:

$$World\ Coordinates = Voxel\ Coordinates \cdot Directions^T + Origin$$

Equation 1: Conversion between voxel coordinates and world coordinates.

The combination of lumen and ILT is used because, in clinical practice, radiologists typically consider the entire vessel when assessing cross-sectional diameters, including the thrombus. By incorporating the thrombus in this calculation, the method maintains consistency with clinical standards and ensures that all measurements reflect the full extent of the vascular lumen and its adjacent structures.

Centerline validation: The centerline shape was validated by superposing it on the 3D segmented structure (*Figure 18, left*), ensuring that all the points of the centerline were located inside the aorta segment separating it symmetrically in the sagittal and coronal view. Additionally, its coordinates were checked by defining key points in the voxel space and confirming that the converted millimeter coordinates matched the 3D Slicer display, which uses millimeter units.

From this centerline, shape features described in *Table 1* are computed:

- **Tortuosity:** the ratio of the actual centerline length to the Euclidean distance between endpoints (*compute_tortuosity*).

---

[2] GitHub repository link: https://github.com/juliaviladelgado/TFG_AAA_Analysis

▪ **Curvature:** local curvature at each point along the centerline, indicating regions of local remodeling (*compute_curvature*) (*Figure 18*), computed using the expression:

$$\kappa(t) = \frac{\parallel r'(t) \times r''(t) \parallel}{\parallel r'(t) \parallel^3}$$

Equation 2: Local curvature expression, where r(t) represents the smoothed 3D centerline, r'(t) and r''(t) are its first and second derivatives with respect to the curve parameter and || || denotes the Euclidean norm.

However, the formula is implemented numerically using centered finite differences via *np.gradient()* on the smooth coordinates.
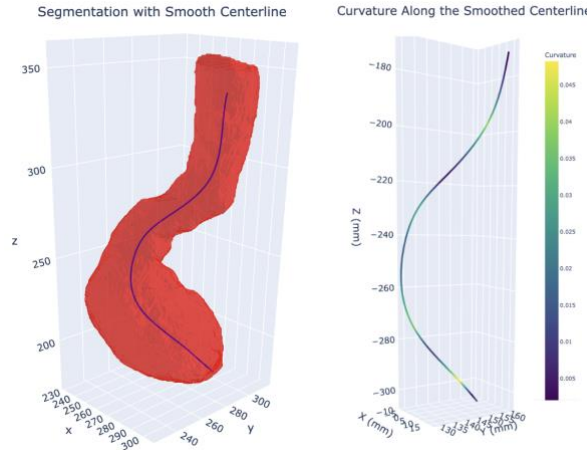
Figure 18: 3D representations of smooth centerline superposed with Lumen + Thrombus segmentation (left) and local curvature along the centerline (right).

The outputs of this block are the tortuosity and the statistical distribution (mean, standard deviation, and maximum) of the curvature along the aortic path.

7.3.2 Cross-sectional Analysis

With the centerline established, it is discretized into equally spaced points every 5mm using the function *discretize_centerline().* At each sampled point, cross-sectional areas, diameter, and circularity for the lumen, ILT, wall, and calcifications are computed. However, due to the complex geometry of the aorta, especially in specific patients with regions of high curvature, unconstrained area extraction could mistakenly include parts of the vessel that belong to adjacent slices. To address this, constrained area extraction is performed: a vessel-wide region of interest (ROI) is first created by using morphological erosion and dilation on the vessel mask (*get_main_island_mask()*). This ensures that only structures physically associated with that centerline point are considered (*Figure 19*). A more detailed explanation of this process is provided in *Annex 2.*
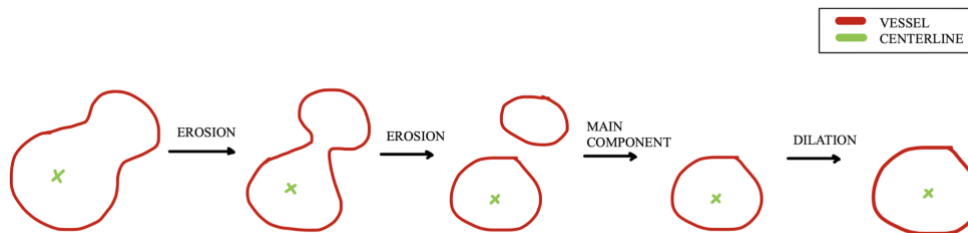
Figure 19: Representation of the process to obtain main component of a binary mask.

Once this main vessel ROI is defined, it acts as a constraint mask for calculating the cross-sectional areas of other segments (lumen, ILT, wall, and calcifications) using the *get_constrained_area()* function.

```
# 3. Calculate area of each segment
for name, mask in segments.items():
    if name == "Lumen_A":
        area, slice_img = get_constrained_area_lumen(mask, point, normal, header,
                                                     constraint_mask=roi_mask,
                                                     grid_size=grid_size, resolution=resolution)
    else:
        area, slice_img = get_constrained_area_others(mask, point, normal, header,
                                                      constraint_mask=roi_mask,
                                                      grid_size=grid_size, resolution=resolution)
```

Figure 20: Python code representing the obtention of cross-sectional areas constrained using the defined ROI.

To compute the cross-sectional area, the tangent vector at each sampled point is used to define a normal vector of the cutting plane (*Figure 21*). Specifically, this tangent vector determines the plane orientation, and a 2D grid in the plane is generated. The intersecting voxels are sampled using nearest neighbor interpolation.
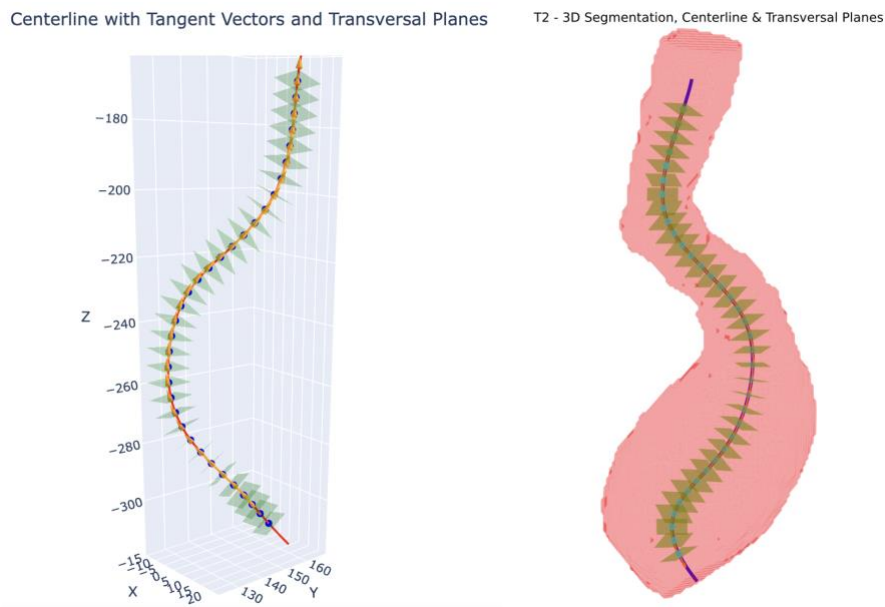
Figure 21: 3D representation of the transversal planes that will be used to compute cross-sectional measures.

Cross-sectional Area Validation: To validate the obtained measurements, 3D Slicer platform was used, which allows for manual cross-sectional area calculation by applying different inclinations. Consistency was demonstrated through multiple verifications.

Additional cross-sectional metrics include:

▪ **Circularity:** calculated using the standard formula (*Equation 3*) through *compute_circularity_from_mask(),* which performs a previous edge smoothing due to interpolation irregularities (*Figure 22*). Circularity quantifies how closely the shape of the cross-section resembles a circle and is related to the stability of the geometrical shape. In this case, the area was recalculated using the Shoelace theorem, a method for calculating the area of polygons from their vertex coordinates (*Equation 4*), to ensure consistency between the area and the smoothed edges and avoiding values greater than 1.

- **Maximum diameter:** the largest distance between points on the cross-sectional contour, as represented in *Figure 22* (*compute_max_diameter_from_mask()*).

$$Circularity = \frac{4\pi \cdot A}{P^2}$$

Equation 3: Circularity formula, where A is the area of the 2D shape and P is the perimeter of its contour.

$$A = \frac{1}{2}\left|\sum_{i=1}^{n} x_i y_{i+1} - y_i x_{i+1}\right|, \quad with \left(x_{n+1,} \ y_{n+1}\right) = (x_{1,} \ y_1)$$

Equation 4: Shoelace theorem. This formula computes the area of a simple polygon defined by ordered points.

Circularity Validation: For circularity validation, a comparative approach was used by comparing slices with more irregular shapes to those with more regular shapes, showing consistently lower or higher circularity values. Additionally, all values were verified to fall within the 0 to 1 range.

Diameter Validation: For diameter measurements validation during the process, the same procedure as for the cross-sectional areas was followed. By manually defining the normal vector (used in the algorithm) in 3D slicer and applying the inclined plane, manually measured diameters showed consistency with those calculated automatically.
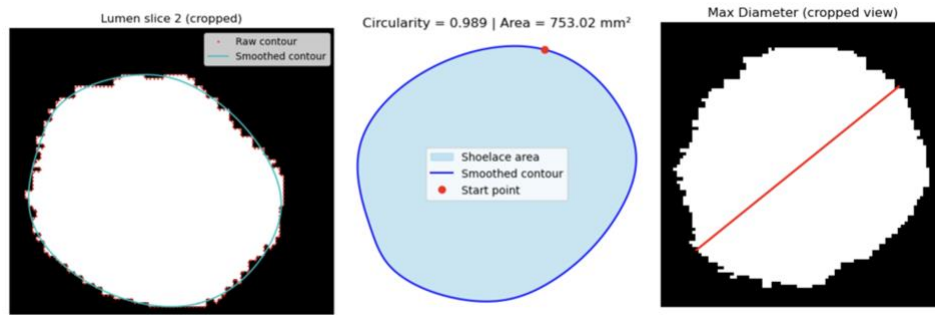
Figure 22: Circularity and maximum diameter representation. Left image: raw and smooth contour of an interpolated cross-sectional slice. Central image: Circularity computation using Shoelace theorem. Right image: Maximum diameter representation.

This block generates longitudinal profiles of these metrics along the centerline, storing them in a dataframe (*df_transversal_profiles*) and generating evolution plots comparing both acquisitions (an example can be seen in *Figure 23*).
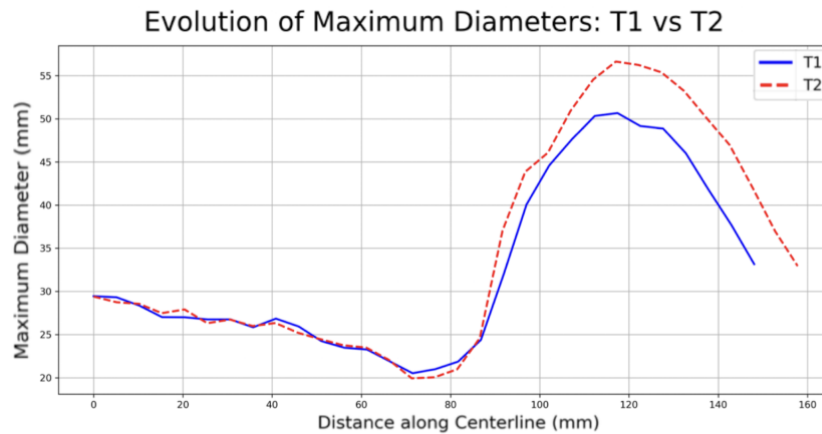
Figure 23: Plot showing the diameter evolution along the centerline between acquisitions.

7.3.3 Volumetric Analysis

This stage involves calculating the volumes of different anatomical regions (lumen, ILT, wall, and calcifications, globally and in IRA/SRA subregions) using the function *compute_segment_volume().* This method considers the voxel spacing defined in the header to ensure accurate volume estimates. It counts all the voxels contained in the segmentation and multiplies by the size of a voxel, storing all volumes in a dictionary.
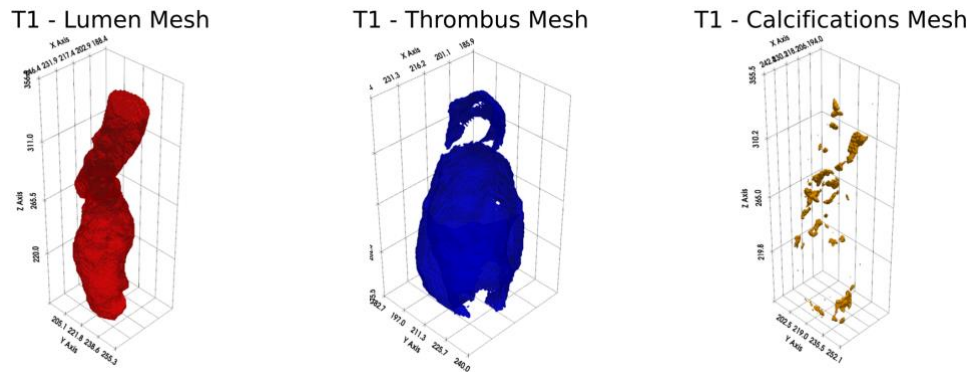
Figure 24: 3D representation of the different segment volumes (lumen, ILT, calcifications, respectively).

It also calculates important volumetric ratios, such as the thrombus-to-lumen ratio in the infrarenal region (IRA), which can have implications for hemodynamic risk and remodeling.

Volume Validation: Volumes can also be calculated automatically with 3D Slicer, yielding the same results as the algorithm-based calculations.

7.3.4 Calcification Analysis

A dedicated analysis of calcifications includes:

- Counting the total number of calcifications (*count_calcifications()*), considering each islet as an isolated calcification.
- Measuring the volume of each calcification (*compute_all_calcification_volumes()*).

Additionally, the average and total volume of all calcifications are reported. These features offer insights into the degree of calcific burden in the aneurysmal wall. In particular, the average volume of calcifications not only indicates the overall extent of calcification but also provides information on whether these calcifications are concentrated in specific areas or more diffusely spread through the wall.

Calcification Validation: Since these measurements are also based on volume analysis, the same tools from 3D Slicer were used to validate.

7.3.5 Contact Area between Thrombus and Wall

An important structural feature is the surface area of contact between the ILT and the aortic wall, which can relate to processes like hypoxia or wall weakening. This is calculated by generating 3D meshes from binary masks (*generate_mesh_from_mask()*) and identifying the areas in close proximity using *compute_contact_area_from_meshes()* A distance threshold is defined and the areas of all triangles within that distance are summed to obtain the total contact area (*Figure 25*). A more detailed explanation of this process is provided in *Annex 3*.
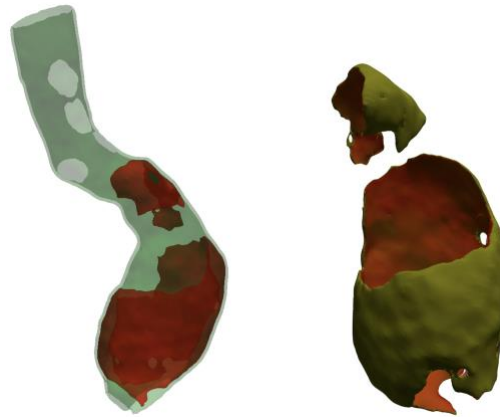
Figure 25: Contact area between thrombus and wall. Left image shows tho segments together (ILT in red and wall in green). Right image represents the ILT with the regions in contact with the wall in green.

Contact Area Validation: Direct validation of the computed contact area was not possible because no external tool was available. However, two indirect checks were performed:

- Contact area visualization in 3D interactive plots confirmed that the contact region was well defined and consistent with the expected anatomy (*Figure 25*).
- The order of magnitude of the computed contact area matched other similar-sized structures, suggesting that the values were realistic.

7.3.6 Radiomic Features

Radiomic descriptors are extracted for two regions of interest:

- **ILT:** Intra Luminal Thrombus
- **PVAT:** Periaortic Adipose Tissue, generated by 1.5mm of isotropic dilation of the vessel mask using *generate_periaortic_mask()*.

The feature extraction uses the *PyRadiomics* library. Extracted features include first-order statistics (mean, skewness, kurtosis, energy) and texture-based features (GLCM, GLRLM, GLDM), reflecting tissue heterogeneity and possible biological processes such as inflammation or thrombus organization.

7.4 Visual Representation of the Features

The output generation step is entirely implemented within the *run_single_patient.py* script. This script runs the extraction pipeline two times (one for each acquisition) by calling the *process_patient()* function and then organizes all the extracted data and measurements in a clear and structured way. Essentially, it is responsible for gathering all the numerical results and creating files and visual reports that can be easily interpreted.

At the start of the script, it is necessary to define the patient identifier (*patient_id*) and the output directory path (*base_dir*) as shown in *Figure 26*. These two parameters make sure that the analysis is applied to the right patient data and that the results are saved in an organized folder structure, in which a folder named with the patient ID will be created.

```
# === CONFIGURATION ===
patient_id = "SP5087"
base_dir = "/Users/juliaviladelgado/Desktop/TFG/3DSlicer/Patient_Analysis"
```
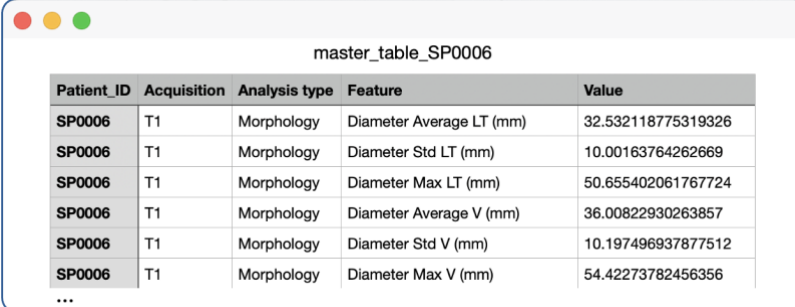
Figure 26: Configuration to be set before running the run_single_patient_.py script.

▪ **Research-Oriented Analysis:** The script creates complete tables containing all the morphological and radiomic data extracted in the previous stage. These tables can be used in future research studies, for example, to compare patient groups, identify trends, or even train predictive models.

▪ **Clinical Application:** The script also produces medical report and figures easy to understand that highlight important changes between the two scans (T1 and T2). Key measurements such as maximum diameters, thrombus changes, and calcification data are summarized and visualized so that they can be reviewed directly by clinicians.

7.4.1 Data Organization: Master and Evolution Tables

The structured data outputs generated by the pipeline are systematically organized into three primary tables stored in *.csv* format:
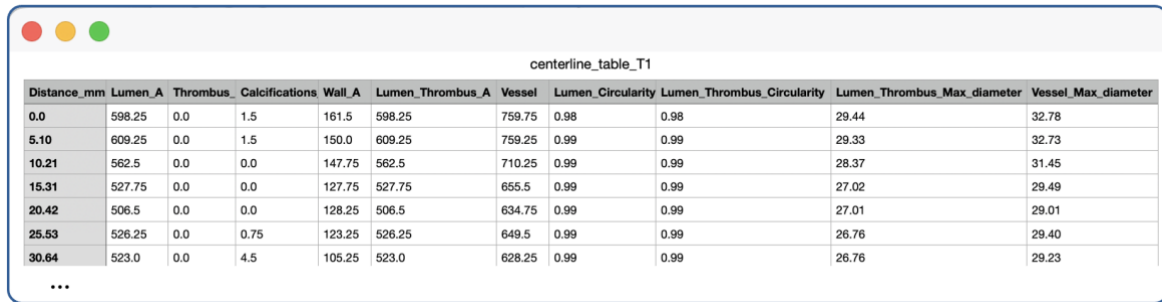
▪ **Master Table** is a comprehensive repository that gathers all the extracted features from both acquisitions (T1 and T2). Each record within this table includes the feature name (e.g., maximum diameter, mean circularity), the patient ID, the acquisition phase (T1 or T2), the corresponding analysis type (such as morphological, radiomic, or volumetric), and the numerical value of the feature. This table is particularly valuable for research purposes, as it provides a standardized and centralized dataset that facilitates large-scale analyses and comparisons across patients.

master_table_SP0006

Patient_ID	Acquisition	Analysis type	Feature	Value
SP0006	T1	Morphology	Diameter Average LT (mm)	32.532118775319326
SP0006	T1	Morphology	Diameter Std LT (mm)	10.00163764262669
SP0006	T1	Morphology	Diameter Max LT (mm)	50.655402061767724
SP0006	T1	Morphology	Diameter Average V (mm)	36.00822930263857
SP0006	T1	Morphology	Diameter Std V (mm)	10.197496937877512
SP0006	T1	Morphology	Diameter Max V (mm)	54.42273782456356
...				

Figure 27: Fragment example of a master table generated by the algorithm.
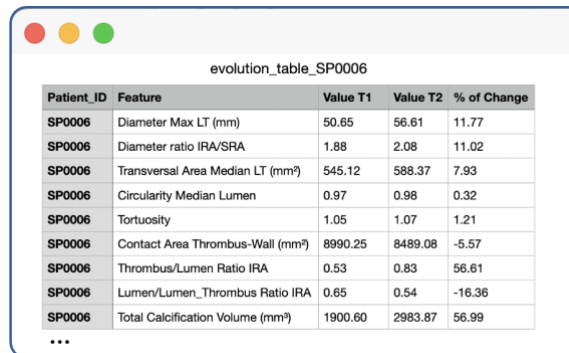
▪ **Centerline Profile Tables** are generated separately for each acquisition. These tables capture detailed point-wise metrics along the discretized centerline, such as the cross-sectional areas of the lumen, thrombus, wall, and calcifications and the diameter and circularity at each sampled location. These granular profiles enable a precise spatial characterization of the vascular morphology and can be used to calculate more complex characteristics implementing additional techniques, such as signal frequency or shape maximum gradient.

Distance_mm	Lumen_A	Thrombus_	Calcifications	Wall_A	Lumen_Thrombus_A	Vessel	Lumen_Circularity	Lumen_Thrombus_Circularity	Lumen_Thrombus_Max_diameter	Vessel_Max_diameter
0.0	598.25	0.0	1.5	161.5	598.25	759.75	0.98	0.98	29.44	32.78
5.10	609.25	0.0	1.5	150.0	609.25	759.25	0.99	0.99	29.33	32.73
10.21	562.5	0.0	0.0	147.75	562.5	710.25	0.99	0.99	28.37	31.45
15.31	527.75	0.0	0.0	127.75	527.75	655.5	0.99	0.99	27.02	29.49
20.42	506.5	0.0	0.0	128.25	506.5	634.75	0.99	0.99	27.01	29.01
25.53	526.25	0.0	0.75	123.25	526.25	649.5	0.99	0.99	26.76	29.40
30.64	523.0	0.0	4.5	105.25	523.0	628.25	0.99	0.99	26.76	29.23
...										

Figure 28: Fragment example of a centerline profile table generated by the algorithm.

- **Evolution Table** is specifically tailored for clinical assessment. It compares a selection of key parameters between the two acquisitions, calculating the percentage changes. This table focuses on features with significant clinical relevance, including maximum diameters and areas, volume ratios (e.g., thrombus-to-lumen), tortuosity evolution, and the number and volume of calcification progression.

Patient_ID	Feature	Value T1	Value T2	% of Change
SP0006	Diameter Max LT (mm)	50.65	56.61	11.77
SP0006	Diameter ratio IRA/SRA	1.88	2.08	11.02
SP0006	Transversal Area Median LT (mm²)	545.12	588.37	7.93
SP0006	Circularity Median Lumen	0.97	0.98	0.32
SP0006	Tortuosity	1.05	1.07	1.21
SP0006	Contact Area Thrombus-Wall (mm²)	8990.25	8489.08	-5.57
SP0006	Thrombus/Lumen Ratio IRA	0.53	0.83	56.61
SP0006	Lumen/Lumen_Thrombus Ratio IRA	0.65	0.54	-16.36
SP0006	Total Calcification Volume (mm³)	1900.60	2983.87	56.99
...				

Figure 29: Fragment example of an evolution table generated by the algorithm.

7.4.2 Automated Generation of Medical Reports

The final step of the pipeline consists of automatically generating a detailed PDF report and several visual plots that can help clinicians and researchers understand the results in a clear way.

The entire process is handled within the *run_single_patient.py* script, which runs a specific block of code at the end to generate the PDF report. In this block, the *subprocess* module is used to run the Quarto rendering command. The report is built using a template file (*report_template.qmd*) that combines Python code with LaTeX for a consistent and professional layout. The script also passes in the patient-specific data and output folders as environment variables to ensure that the report is tailored to the particular patient.

Annex 4 provides an example of a complete report; each patient report includes:

- A table that summarizes how key features change between the two scans (*evolution_table*).
- 3D images of the segmentations and centerline, showing the transversal planes at each point along the vessel.
- Plots that show the maximum diameter changes and transversal areas of the different segments along the vessel centerline.
- 3D mesh visualizations of each segment (lumen, thrombus, and calcifications), shown separately and together.

- Tables with the most clinically relevant numerical results, including volume changes and diameter metrics.

Besides the PDF report, the pipeline saves all the plots it creates in their corresponding folder for T1 and T2.

7.5 Result Validation and Analysis

7.5.1 Accuracy and Consistency in Diameter Measurements

Since the maximum diameter is the only metric directly comparable with the clinical reports, an assessment was conducted to determine the reliability of the automatically extracted values. Several error and correlation metrics were calculated, yielding the following results in *Table 2*.

Metric	Value	Metric	Value
Mean Absolute Error (MAE)	1.9 mm	Median Absolute Error	1.55 mm
Root Mean Square Error (RMSE)	2.2 mm	Standard Deviation	1.26 mm
Mean Absolute Percentage Error (MAPE)	3.9%	Pearson Correlation Coefficient	0.975

Table 2: Summary of regression metrics for model performance evaluation.

These findings indicate a high level of agreement between the automatically and manually measured diameters. Most absolute errors are below 2 mm, and the percentage error remains under 4%. The near-perfect Pearson correlation further supports a strong linear relationship between manual and automatic measurements. This suggests that the automated pipeline reliably reproduces the key diameter metric used in clinical practice.

On the other hand, in the initial phase of the analysis, patients were classified into two growth categories ("slow" and "rapid") based on the manually measured diameter reported by clinicians in the medical records. To assess the robustness of the automated diameter extraction pipeline, the same classification criteria were applied using the automatically calculated diameter velocities, ensuring that both classification processes shared identical thresholds for categorizing growth speed. In this case, patients that showed a growth rate < 2 mm/year were considered slow growth and patients with a growth rate of >4 mm/year were in the "rapid" group.

The classification between manual and automatic classifications is summarized in the confusion matrix shown in *Figure 30*. This matrix reveals perfect agreement between the two approaches, with all patients consistently classified into the same category by both the manual and automated methods. Specifically, 5 patients were classified as "slow growth" and 5 as "rapid growth".
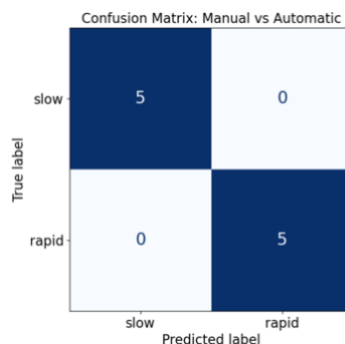
Figure 30: Confusion matrix showing patient classification according to manual vs. automatic growth rate computation.

One minor discrepancy was observed: one patient had an automatically calculated growth rate of 2.1 mm/year, just above the 2 mm/year threshold. As this value was very close to the slow growth limit and far from the rapid growth threshold of 4 mm/year, it was pragmatically assigned to the slow growth. This decision is further justified by the fact that these thresholds were arbitrarily defined within this exploratory study, serving more as practical cutoffs rather than statistically validated boundaries.

7.5.2 Relationship Between Diameter and Volume

To further investigate the relationship between the change in diameter and the corresponding change in volumes in the evolution of aneurysms, a scatter plot was generated (*Figure 31*). In this plot, each point represents a measurement (T1 or T2) for each patient, showing the maximum diameter and the volume of the lumen plus thrombus in the infrarenal aorta segment.
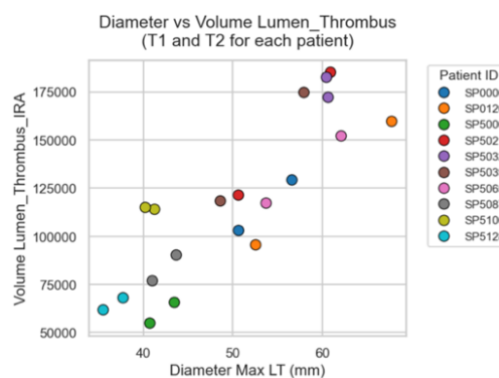
Figure 31: Plot showing maximum diameter in the Lumen + ILT segment vs. the volume in the infra-renal region. Each point represents a patient and an acquisition.

Initially, a clear linear relationship is observed between diameter and volume values, the higher the diameter, the higher volume. But also, this plot highlights an important observation: while the maximum diameter is the clinically used parameter to classify and monitor aneurysm evolution, patients with similar diameters can have significant differences in the volume of the aneurysmal segment. For example, patients SP5006, SP5106, and SP5087 all have similar diameters, yet their corresponding volumes highly differ, some showing nearly double the volume of others.

A similar pattern can be observed in the case of patients SP0006 and SP5039. While both exhibit a similar increase in diameter, the patient SP5039 shows a much larger increase in the volume of the lumen plus thrombus compared to SP0006.

7.5.3 Lumen and Thrombus Volume Changes in Slow Growth Subjects

The aim was to investigate if in the slow growth group, although diameter is not changing, there could be other parameters that were increasing or decreasing, changing aneurysm's geometry and composition. Most of the parameters stayed stable, but slight changes were observed, for example, as observed in *Figure 32,* in the case of the volume of lumen and thrombus for a specific patient. It was analyzed using scatter plots of T1 versus T2 volumes. The total volume of the lumen + thrombus remains unchanged over time for all the patients, consistent with the observation that the maximum diameter also shows minimal variation in this group. However, in the case of SP5106 individual components of this total volume (lumen and thrombus separately), show opposite trends: while the lumen tends to decrease slightly, the thrombus volume correspondingly increases.
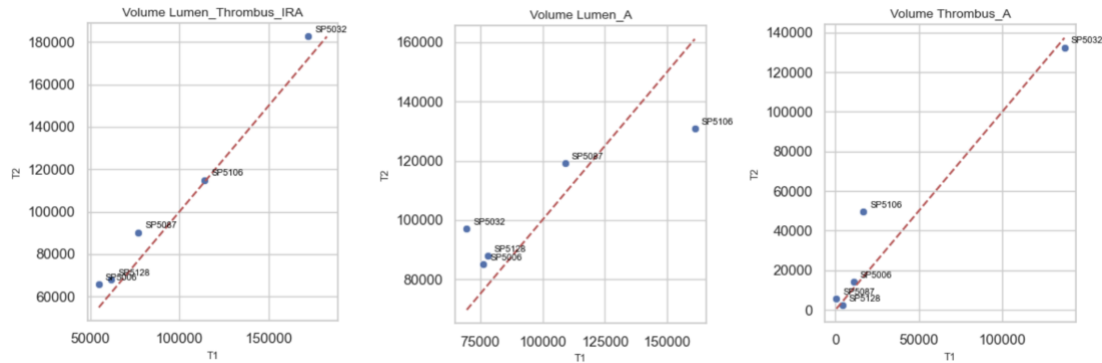
Figure 32: Plot representing Lumen + ILT, Lumen and ILT volume changes between T1 and T2 for the slow growth group.

7.5.4 Exploratory Analysis of Feature Evolution

To further explore morphological changes across growth rates, boxplots were generated showing the distribution of the percentage of change in each feature, separated by growth group.The plots suggests that the "rapid" group generally exhibits larger median changes in other key features rather than just diameter measurements, including transversal areas, which are directly related to the diameter, but also in circularity, calcification metrics and volume measures. This indicates that, besides diameter, there are also other parameters that are changing. Although these trends are interesting and seem to align with morphological evolution in rapidly growing aneurysms, it is important to note that this analysis is purely exploratory due to the small patient sample size.
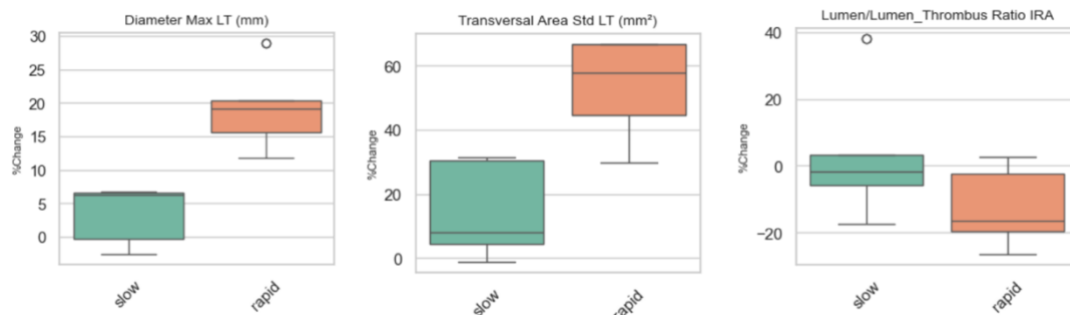
Figure 33: Boxplots representing % of change of different measures (Max diameter, Transversal Area Standard Deviation and Volume Ratio between Lumen and Lumen + ILT), separated by slow (green) and rapid (orange) growth groups.

However, some inconsistencies were also observed in the data. For example, in certain patients, some volumetric measurements, specifically in calcifications, appear to decrease over time (as seen in *Figure 34*), which is not accepted in the literature as a natural progression of the AAA, indicating a certain bias in some part of the pipeline.
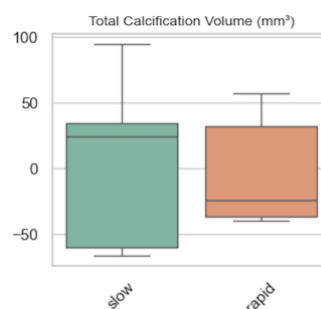
Figure 34: Boxplots representing a decreasing % of change of total calcification volume, separated by slow (green) and rapid (orange) growth groups.

7.5.5 Baseline Feature Differences by Growth Group

To better understand how aneurysm characteristics might differ between the slow and rapid growth groups, we generated boxplots for each parameter using data from the baseline acquisition (T1), represented in *Figure 35*. As explained earlier, even though the number of patients in this study is small and this analysis is only exploratory, some trends were noticeable.

For example, the median circularity of the lumen seems to be a bit lower in the rapid growth group, which might suggest a more irregular shape. Tortuosity, while not drastically different, tends to be higher in the rapid growth group, which could mean a more winding or twisted shape of the vessel. The thrombus-wall contact area also tends to be higher in this group, suggesting a possibly larger area of thrombus attached to the vessel wall, causing it hypoxia, and weakening it.

Other features, like thrombus-to-lumen volume ratios and the total calcification volume, also appear higher in the rapid group, but there is a lot of variability, especially for the calcifications. Radiomic features of the thrombus, such as skewness, kurtosis, and run-length non-uniformity, also show higher values in the rapid growth group, which could indicate differences in texture.

To assess whether these differences were statistically significant, a Mann-Whitney U test for each feature was performed. However, none of the p-values were below the 0.05 threshold.

It's important to note that these observations are just descriptive. Because of the small number of patients and lack of statistical testing, we cannot draw any solid conclusions.

The following figures show the most representative boxplots, illustrating these trends visually.
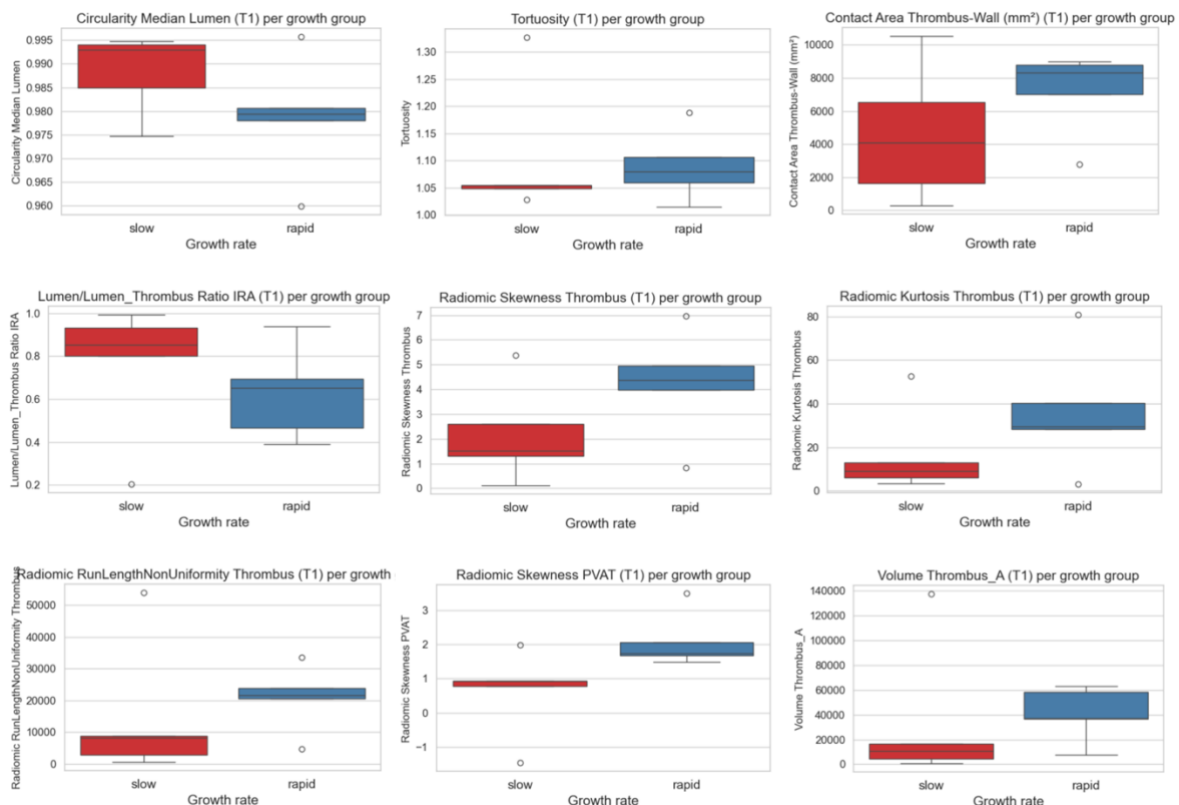
Figure 35: Boxplots for different parameters using data from the baseline acquisition (T1), separating between rapid (blue) and slow (red) growth rates.

8. DISCUSSION

8.1 Property Extraction Pipeline Consistency

The methodology developed in this project has proven its capability to automate the extraction of morphological and radiomic features from CT images with AAA. The modular structure of the pipeline, which includes from the data acquisition, preprocessing and segmentation, to feature extraction and result generation, has allowed for a systematic analysis of the complex vascular geometry and associated texture patterns.

One of the key strengths of this pipeline is its completely automated structure, which ensures reproducibility and consistency across patients. Thanks to the open-source software tools implemented (such as 3D Slicer, PyRadiomics and custom Python scripts), the workflow is transparent and can easily be adapted to different clinical or research environments. Moreover, the validation of intermediate steps (like centerline geometry, transversal areas, or volumes) through comparisons with manual measurements in 3D Slicer has reinforced confidence in the reliability of the automated calculations.

The decision to segment the four key vascular components (lumen, ILT, wall, and calcifications) and analyze their spatial and radiomic properties separately provides a more nuanced view of AAA morphology than using diameter alone. The segmentation process was standardized and reviewed by clinical staff to guarantee methodological consistency, even though segmentations were generated manually. This highlights both a strength and a limitation: while manual segmentation enables detailed anatomical accuracy, it also introduces potential operator-dependent variability. Future integration of semi-automatic or AI-based segmentation methods could reduce this variability, streamline the workflow, and increase scalability.

The success of the methodology in this proof-of-concept study is notable. Among the 10 selected patients, the pipeline produced consistent and coherent results, with all stages functioning reliably and the output metrics showing agreement with manual validations. However, it is important to note that this sample may not fully represent the broader spectrum of AAA presentations. When applied to a larger and more diverse patient population, it is likely that more complex geometries and edge cases will emerge that could challenge specific components of the pipeline. For this reason, additional validation on a larger cohort is essential, which could reveal specific limitations and inform necessary adaptations to improve generalizability and robustness.

In addition, while the extracted features provide rich morphological and radiomic information, their clinical interpretability and predictive value have not been fully explored yet. The exploratory analyses suggest potential associations between features and aneurysm growth patterns, but further statistical modeling and validation studies are needed to confirm their relevance.

8.2 Clinical Implementation

The results obtained in this project, based on an automated pipeline for the extraction of morphological and radiomic features to characterize aneurysms from CT images, provide a first indication of the feasibility and coherence of the proposed methodology.

Firstly, the comparison between maximum diameter automatic measurements and the manual ones reported in the clinical reports show a very high level of agreement, with a mean absolute

error lower than 2mm and a Pearson correlation coefficient higher than 0.97. These data support reliability of automatic diameter extraction, and can be a robust alternative to manual measurements, optimizing time and reducing inter-observer variability. However, there is still some discrepancy, no matter how small, between manual and automatic measurements. It is not possible to determine whether this difference is due to the inherent subjectivity of manual measurements or to limitations in the algorithm itself.

Regarding growth classification, the perfect consistency between manual and automatic methods in assigning patients to slow and rapid growth groups further support the robustness of the pipeline in identifying general growth patterns.

8.2.1 Exploration of Future Biomarkers

The exploratory analysis of the evolution of various features showed that the patients in the "rapid" growth group tend to show higher changes in other metrics beyond maximum diameter. Notably, these included cross-sectional areas, circularity and metrics related to calcifications. These findings suggest that, in patients with fast evolution of the aneurysm, there exists a geometrical and structural remodeling more complex that could not be captured with the maximum diameter alone.

Furthermore, the analysis of baseline differences (T1) between the two growth groups revealed that some metrics, such as lumen circularity, tortuosity, contact area between thrombus and wall and volumetric proportions, tend to be higher in the rapid growth group. Other differences in radiomic features were identified as well, related with the thrombus (skewness, kurtosis, run-length non-uniformity), which could suggest textural differences among different groups. Nonetheless, the p-values observed were above the threshold, indicating a lack of statistical significance. However, these early findings do suggest that there could be morphological and radiomic markers related to growth speed, which would be interesting to explore in larger studies.

At the same time, the relationship between diameter and volume showed that, although these patients would be classified equally due to similar diameter measures, the actual volume of the aneurysm can be very different. Knowing these differences could help to develop more personalized risk assessments, make predictions on how it will evolve, and decide on treatments. These observations could highlight the importance of using three-dimensional metrics like volume to better capture the complex geometry of aneurysm evolution, rather than relying only on diameter measures.

In the slow growth group, although global variations were small, cases were identified where there was an internal volumetric redistribution between lumen and thrombus, suggesting a possible internal redistribution of the aneurysmatic sac without a significative change in maximum diameter. This finding is coherent with the literature, which highlights that the structural and biological heterogeneity if the ILT as an aneurysm evolution modulator. These patterns, although derived from a small exploratory cohort, suggest the possibility of an evolving internal redistribution space within the aneurysm sac that is not captured in clinical reports focusing only on maximum diameter. This internal remodeling, if confirmed in larger studies, could serve as an early indicator of future aneurysm instability or growth.

Additionally, these automated features and morphological insights could be valuable for enhancing clinical decision making in the future. For example, in cases where the maximum diameter is not

beyond surgery limits or it does not show significant changes over time, yet other parameters such as cross-sectional areas, circularity, thrombus-wall contact area or radiomic parameters demonstrate notable alterations, these metrics could act as early biomarkers of accelerated growth or remodeling. Such findings might indicate the need for closer follow-up or proactive interventions, even if the maximum diameter remains stable. Moreover, the combination of geometric and radiomic markers could support more personalized risk assessment and treatment planning, tailoring clinical decisions to the individual patient's vascular morphology and remodeling patterns.

Overall, the results suggest that the automated pipeline reliably reproduces key morphological metrics and offers potential for detecting differential patterns of vascular remodeling. However, due to the small sample size and the absence of formal statistical analysis, these tendencies must be interpreted only as preliminary observations.

8.2.2 Future Lines

Nonetheless, limitations of the study need to be considered. The small sample size and the exploratory nature of the analysis restrict the possibility of establishing solid and generalizable conclusions. Additionally, some contradictory results, like decreases in volumes observed in specific cases, especially in calcification were identified. Since calculating volumes is a very straightforward process, simply counting the voxels and multiplying them by their physical volume, and the results have been checked with other automated software platforms, it seems likely that these discrepancies are due to the segmentation methodology itself. In the case of calcifications, for example, a threshold was manually set to include all visible calcifications, which could lead to variability. This highlights the need of automatic segmentation methods and less user-dependent, possibly based on artificial intelligence, to improve consistency and reproducibility of the derived metrics.

Besides these limitations, the results offer preliminary evidence which supports the hypothesis that morphological and radiomic metrics, beyond maximum diameter, can capture relevant aspects of the aneurysm evolution. These findings suggest future lines of research, such as expanding the cohort to statistically validate these trends and exploring the utility of radiomic and geometric metrics as potential risk predictors.

9. TECHNICAL VIABILITY

This section presents a SWOT (Strengths, Weaknesses, Opportunities and Threats) analysis to evaluate the feasibility and potential impact of the developed pipeline. It provides a comprehensive overview of the technical, clinical, and organizational factors that could influence the adoption and future development of the methodology. This analysis helps to identify key aspects that support the project's viability as well as changes and external factors that must be considered for successful clinical translation.

Strengths	Weaknesses
 - Use of advanced image processing techniques to extract quantifiable features. - Innovative perspective that could improve AAA evaluation. - Result validation with expert radiologists, ensuring clinical reliability. - Development of an automated pipeline that is able to optimize the diagnostic time. - Use of real patient data, increasing clinical applicability.	- Need of a high computational power for medical image processing. - Possible difficulty in precise segmentation due to anatomic variability between patients. - Dependance on the availability of high-quality images for the analysis. - Limited validation due to the availability and accessibility of radiologists to verify results. - Limited time available for analysis and further applications of this methodology need to be explored in future studies, as this work only focused on technical validation and feasibility.
Opportunities	Threats
 - Growing interest in image processing techniques in medicine. - Possibility of integration with computer assisted diagnostic tools in hospitals. - Pipeline expansion to other pathologies related to the aorta. - Collaboration opportunity with other medical centers and universities to expand the project's scope.	- Strict regulations about the use of medical data and patient's privacy. - Possible rejection of the medical community if the results don't show enough reliability. - Fast technology evolution, which could make the pipeline obsolete in a few years. - Difficulty on the clinical implementation due to the resistance to change in hospitals.

Table 3: SWOT analysis representing the project's strengths, weaknesses, opportunities, and threats.

10. EXECUTION SCHEDULE

10.1 Work Breakdown Structure (WBS)

Work Breakdown Structure is a tool that breaks the work into smaller tasks to make the work more manageable and approachable. It is basically a hierarchical decomposition of a project into smaller components. It allows to sort and classify the different tasks under a hierarchical order in which they need to be fulfilled so the objectives and scope of the project is reached. The WBS of this project is represented in *Figure 36*.
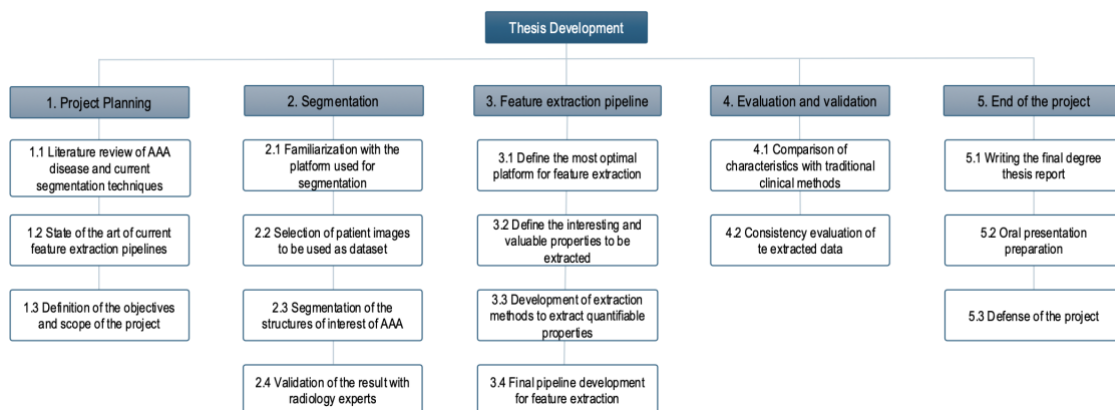
Figure 36: Work Breakdown Structure (WBS) of the project.

This project is composed of 6 work packages with each corresponding task description and duration (in days) represented in the WBS dictionary in *Table 4.*

WBS ID	Task name	Task Description	Duration
WP1. Project Planning			
1.1	Literature review	Literature review of AAA disease and current segmentation techniques	4
1.2	State of the art	Research on the state of the art of current feature extraction pipelines	5
1.3	Project definition	Definition of the objectives and scope of the project	2
WP2. Segmentation			
2.1	Platform familiarization	Familiarization with the platform used for segmentation	5
2.2	Dataset selection	Selection of patient images to be used as dataset	2
2.3	Segmentation	Segmentation of the structures of interest of AAA	30
2.4	Validation	Validation of the results with radiology experts	2
WP3. Feature Extraction Pipeline			
3.1	Platform selection	Definition and familiarization of the most optimal platform for feature extraction	2
3.2	Features to extract	Define the interesting and valuable properties to be extracted	2
3.3	Extraction methods	Development of extraction methods to extract quantifiable properties	30
3.4	Final pipeline	Final pipeline definition and development for feature extraction	10
WP4. Evaluation and Validation			
4.1	Comparison with traditional methods	Comparison of characteristics with traditional clinical methods	8
4.2	Consistency evaluation	Consistency evaluation of the extracted data	5
WP5. End of the Project			
5.1	TFG writing	Writing the final degree thesis report	5
5.2	Oral presentation preparation	Preparation of the oral presentation of the project	5
5.3	Project defense	Defense of the project in front of the tribunal	1

Table 4: Task descriptions and deliverables for the completion of the project.

10.2 PERT Diagram

PERT (Program Evaluation and Review Technique) is a tool used to meticulously program, organize and plan the tasks of a project. It consists of a visual representation of the project chronogram and the dependencies that exist between different tasks as well as identifying the critical path, which any delay of a critical activity would cause a delay on the project. PERT diagram will help to optimize the project's timings.

PERT (Program Evaluation and Review Technique) is a project management tool that allows to efficiently plan and coordinate the different tasks needed to complete the project before the stablished deadline. Its utility focuses on the ability to graphically represent the sequence of activities, identifying dependencies and determining the critical path, composed by those tasks that cannot be delayed without affecting on the total duration of the project.

Before the PERT diagram is developed, a table summarizing project durations and dependencies is made (*Table 5*).

WBS ID	PERT ID	Previous Task	Duration (days)
1.1	A	-	4
1.2	B	A	5
1.3	C	B	2
2.1	D	C	5

2.2	E	C	2
2.3	F	D, E	30
2.4	G	F	2
3.1	H	C	2
3.2	I	H	2
3.3	J	G, I	30
3.4	K	J	10
4.1	L	K	8
4.2	M	K	5
5.1	N	L, M	5
5.2	O	N	5
5.3	P	O	1

Table 5: Identification, dependencies, and timing of tasks.

From the information summarized in *Table 5,* the PERT diagram is created, represented in *Figure 37.* In this diagram, each arrow represents a specific task of the project, and each node shows the dependencies between them. Furthermore, early, and late time were computed for each task. Early time indicates the minimum time needed to complete a task, while late time is the maximum time in which the activity needs to be fulfilled without causing any delay on the global project duration.

The PERT diagram analysis shows that the critical path, represented by red arrows, is composed by activities A, B, C, D, F, G, J, K, L, N, O and P. This means that a delay in any of these activities would directly impact in the project's end date. On the other hand, activities E, H, I and M provide a certain flexible margin, allowing for a 3-, 33-, 33- and 3-day delay, respectively, without compromising the project timing. The total estimated duration of the project is of 107 days, and any deviation from the original plan of the critical activities would cause a delay in the final duration.

Figure 37: PERT diagram of the project.

This planning reflects the logical structure of the project. Before starting the project's development, a bibliographic review and definition of the project's objectives are mandatory. Once these aspects are completed, familiarization with the tools and platforms needed for segmentation and image processing is carried out. Segmentation and validation phases require a significative dedication, which involves the interaction with experts to guarantee result precision. Next, feature extraction and pipeline construction are developed. Finally, thesis redaction and oral presentation preparation compose the final step of the project.

10.3 GANTT Diagram

GANTT diagram is a tool that allows to visualize in a clear and structured way the temporal planning of the different tasks. It is a graphical representation in which each activity is displayed as a bar, showing its duration, margin, and relation with the other tasks of the project.

This diagram facilitates the dependencies identification between activities and helps manage the execution time of each work phase. Furthermore, it allows for a tracking project process, ensuring al deadlines are fulfilled.

In *Figure 38*, the GANTT diagram for this project is shown, developed using the information obtained with the PERT diagram. A chronical organization of the different tasks can be observed as well as the precedence relationships between them.
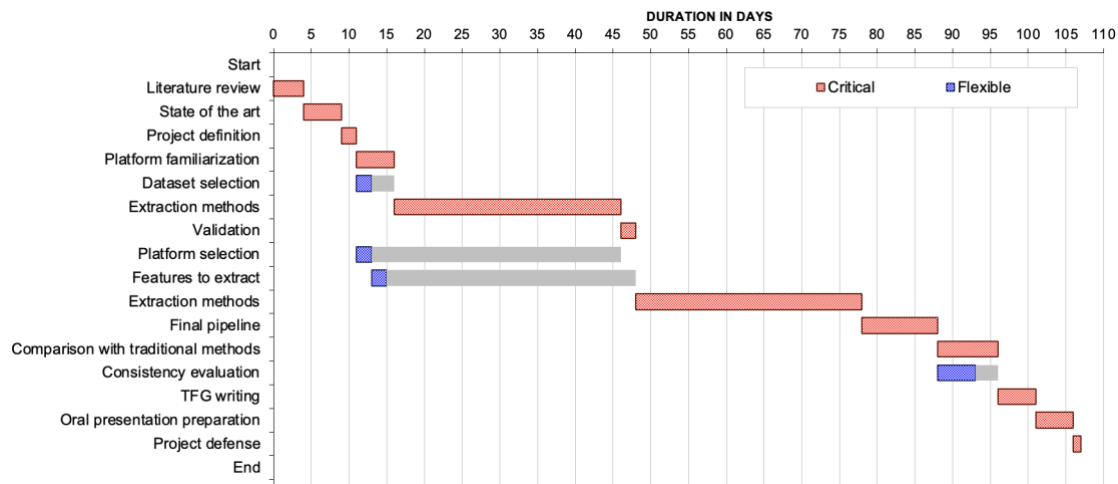
Figure 38: GANTT diagram of the project.

11. ECONOMIC VIABILITY

The economic viability analysis estimates the resources and costs needed to develop the project, integrating both the computational and experimental tasks carried out at home and at the research institute of the Hospital de Sant Pau. Although the images and most of the software infrastructure were already available, this section identifies the main components contributing to the final budget.

11.1 Material, Software and Licenses Resources

The project used open-source or free tools, including Python, 3D Slicer, BOA software and PyRadiomics. Additionally, the Visual Studio Code (VS Code) environment was used. For advanced image processing, a high-performance workstation (approx. 3500€) was employed at the Institut de Recerca at Hospital de Sant Pau. Since this workstation was already available as a shared resource, its cost is included as an indicative reference of the infrastructure used.

Item	Units	Price/Unit (€)	Total Price (€)
VS Code	1	0	0
3D Slicer	1	0	0
Python	1	0	0
PyRadiomics	1	0	0
BOA software	1	0	0

High-performance workstation (IR)	1	3500	3500
Total			**3500 €**

Table 6: Costs derived from material, software, and licenses resources.

11.2 Subject Related Resources

The project used CT images from patients in the hospital's existing database. Since this data had already been acquired for clinical purposes and was provided to the project by the hospital, no new patient-related costs have been considered. Therefore, the total cost of subject related resources is zero.

Item	Units	Price/Unit (€)	Total Price (€)
CT images (hospital DB)	20	0	0
Total			**0 €**

Table 7: Costs derived from subject related resources.

11.3 Human Resources

Human resources are one of the main costs of the project, including time spent by the student, the thesis tutor (PhD student) and the thesis director. The student is not paid, but a nominal hourly rate of 11€/hour (typical of an undergraduate engineer's salary) is considered for reference. The tutor and director are estimated based on typical hourly rates in Spain considering 15€/h for the PhD student and 20€/h for the thesis director.

The total hours for each role have been calculated as follows: The project spanned 107 working days. The student dedicated 6 hours per day, resulting in 642 hours in total. The PhD student dedicated to the project an average of 10 hours per week, equivalent to 2 hours per day, yielding 214 hours overall. The thesis director contributed approximately 4 hours per week, which corresponds to 0.8 hours per day, adding up to 86 hours over the course of the project.

Staff	Total Hours	Cost/Hour (€)	Total Cost (€)
Student	642	11	7062
PhD Student	214	15	3210
Thesis Director	86	20	1720
Total			**11992 €**

Table 8: Costs derived from human resources.

11.4 Total Costs

Finally, all the costs are summarized to estimate the overall budget for the project.

Sector	Cost (€)
Material, Software & Licenses	3500
Subject Related	0
Human Resources	11992
Total Estimated Cost	**15492 €**

Table 9: Total costs of the project.

12. REGULATIONS AND LEGAL ASPECTS

The project was mainly conducted in Barcelona (Spain), using preexisting CT images of patients at Hospital de Sant Pau. Although no new patient experiment or clinical trials were performed, various regulations and ethical considerations have been taken into account to ensure legal and ethical compliance throughout the project.

12.1 Protection of Patient Data

The processing of patient data in the European Union (EU) is regulated by the General Data Protection Regulation, Regulation (EU) 2016/679 [18], which establishes strict rules guidelines for the collection, use and storage of personal data. This regulation requires that personal data is handled lawfully, transparently, and safely, ensuring confidentiality and integrity of patient data. Moreover, in Spain, the Organic Law 3/2018 on the Protection of Personal Data and Guarantee of Digital Rights (LOPDGDD) complements the GDPR by adding further guidelines to protect data in the healthcare sector [64].

In this project, the data used comes from a previously existing database and it has been anonymized for the proper use in the study. The access to this data has been limited to authorized researchers, ensuring compliance with current regulations and data security.

12.2 Ethical Considerations in Medical Research

Although this project does not include direct intervention with patients, fundamental ethical principles are still applied in the use of clinical data. The Declaration of Helsinki (World Medical Association, 2013) sets key ethical principles for research using patient data, even when there is no direct contact [65]. These principles include the respect for privacy, data confidentiality, and transparency in result communication.

12.3 Regulations on Software and Medical Devices

Although this project focuses on the development of an algorithm for image analysis in research, it is relevant to mention the Regulation (EU) 2017/745 on Medical Devices (MDR), which establishes the requirements for CE marking and approval of medical software when used for clinical or diagnostic purposes [66]. In this case, the algorithm developed has been used only for research and proof-of-concept purposes, so it does not require certification as a medical device. However, if the algorithm were to be integrated into clinical practice in the future, it would be necessary to comply with MDR and quality management standards such as ISO 13485:2016 [67].

12.4 Quality Standards and Data Management

This project follows practical recommendations for quality management of data and integrity, in line with ISO 27001:2013, which establishes requirements for the safe management of information, especially relevant in contexts where sensitive data like medical images is involved [68]. Additionally, basic data quality and traceability principles have been followed according to ISO 9001:2015, although without a formal certification [69].

12.5 Future Considerations and Transparency

Given that this project represents an initial step to validate a feature extraction algorithm, it is essential to guarantee transparency and replicability in results. Any future application in clinical

environments should additionally consider external validation studies and conformity with data protection legislation and medical software regulation before its implantation in healthcare practice.

13. CONCLUSIONS

This study demonstrates the feasibility and coherence of an automated pipeline for the extraction of morphological and radiomic features from CT images of abdominal aortic aneurysms (AAA). The methodology, which used open-source tools and custom Python scripts, has proven to be a promising approach for detailed AAA characterization, showing equilibrium between automation and flexibility and achieving high agreement with manual evaluations performed by experts.

By combining the segmentation of key vascular structures with a wide range of quantitative analyses, the pipeline enables a multidimensional assessment of aneurysm anatomy and evolution. The consistency of results across the selected patient sample supports its robustness and the validity of its intermediate calculations.

Despite the success in the current proof-of-concept, the small sample size presents a major limitation. The absence of statistically significant differences between patient groups may result from insufficient statistical power, or it may suggest that the observed trends are not strong enough in this dataset. For this reason, the findings should be interpreted with caution, as they may be influenced by individual variability or operator-dependent segmentation. Nevertheless, the exploratory observations suggest potentially relevant biomarkers, such as circularity, thrombus-wall contact area and radiomic descriptors, that could be associated with aneurysm growth dynamics.

Importantly, the analysis revealed that volume and morphological features can differ even between patients with similar diameters, and that internal remodeling processes can occur without diameter progression. These findings support the idea that relying exclusively on maximum diameter may not be enough to capture the full complexity of AAA evolution.

Further research is necessary to validate these results in larger cohorts, improve the segmentation process through AI-based automation, and evaluate the predictive value of the extracted features. These steps would not only improve the reliability and scalability of the pipeline, but also move it closer to translational clinical applications, enabling more personalized and accurate risk stratification in vascular medicine.

In summary, this work opens new perspectives for a more comprehensive and robust characterization of AAA and contributes to the ongoing efforts to improve early detection, monitoring, risk prediction, and treatment decision making in patients with abdominal aortic aneurysms.

14. REFERENCES

[1] Golledge, J., Thanigaimani, S., Powell, J. T., & Tsao, P. S. (2023). Pathogenesis and management of abdominal aortic aneurysm. *European heart journal*, *44*(29), 2682–2697. https://doi.org/10.1093/eurheartj/ehad386

[2] Haller, S. J., Azarbal, A. F., & Rugonyi, S. (2020). Predictors of Abdominal Aortic Aneurysm Risks. *Bioengineering (Basel, Switzerland)*, *7*(3), 79. https://doi.org/10.3390/bioengineering7030079

[3] Moll, F. L., Powell, J. T., Fraedrich, G. *et al.* Management of abdominal aortic aneurysms clinical practice guidelines of the European society for vascular surgery. *European journal of vascular and endovascular surgery : the official journal of the European Society for Vascular Surgery*, *41 Suppl 1*, S1–S58. https://doi.org/10.1016/j.ejvs.2010.09.011

[4] Roychowdhury, T., Klarin, D., Levin, M.G. *et al.* Genome-wide association meta-analysis identifies risk loci for abdominal aortic aneurysm and highlights PCSK9 as a therapeutic target. *Nat Genet* **55**, 1831–1842 (2023). https://doi.org/10.1038/s41588-023-01510-y

[5] Abbasian Ardakani, A., Bureau, N. J., Ciaccio, E. J., & Acharya, U. R. (2022). Interpretation of radiomics features-A pictorial review. *Computer methods and programs in biomedicine*, *215*, 106609. https://doi.org/10.1016/j.cmpb.2021.106609

[6] TeachMeAnatomy. (June, 2025). *Blood vessels – Ultrastructure*. https://teachmeanatomy.info/the-basics/ultrastructure/blood-vessels/#section-67e8332cb747f

[7] Radiology Key (n.d.). *Abdominal aorta*. Radiology Key. https://radiologykey.com/abdominal-aorta-5/

[8] Haller, S. J., Azarbal, A. F., & Rugonyi, S. (2020). Predictors of Abdominal Aortic Aneurysm Risks. *Bioengineering (Basel, Switzerland)*, *7*(3), 79. https://doi.org/10.3390/bioengineering7030079

[9] University of Chicago Medicine. (n.d.). *Abdominal Aortic Aneurysm.* https://www.uchicagomedicine.org/conditions-services/heart-vascular/aortic-disease/abdominal-aortic-aneurysm.

[10] Roychowdhury, T., Klarin, D., Levin, M.G. *et al.* Genome-wide association meta-analysis identifies risk loci for abdominal aortic aneurysm and highlights PCSK9 as a therapeutic target. *Nat Genet* **55**, 1831–1842 (2023). https://doi.org/10.1038/s41588-023-01510-y

[11] Chaikof, E. L., Dalman, R. L., Eskandari, M. K. et al. (2018). The Society for Vascular Surgery practice guidelines on the care of patients with an abdominal aortic aneurysm. *Journal of vascular surgery*, *67*(1), 2–77.e2. https://doi.org/10.1016/j.jvs.2017.10.044

[12] Standford Health Care. (n.d.). *Abdominal aortic aneurysms: Treatments.* https://stanfordhealthcare.org/medical-conditions/blood-heart-circulation/abdominal-aortic-aneurysm/treatments.html

[13] Bartolozzi, C., Neri, E. & Caramella, D. (2019). CT in vascular pathologies. *European Radiology* 8, 679–684. https://doi.org/10.1007/s003300050459

[14] Stiller, W. (2018) Basics of iterative reconstruction methods in computed tomography: A vendor-independent overview. *European Journal of Radiology*. 109, 147–154. https://doi.org/10.1016/j.ejrad.2018.10.025

[15] Doyle, B. J., Bappoo, N., Syed, M. B. J. et al. (2020). Biomechanical Assessment Predicts Aneurysm Related Events in Patients with Abdominal Aortic Aneurysm. *European journal of vascular and endovascular*

surgery : the official journal of the European Society for Vascular Surgery, 60(3), 365–373. https://doi.org/10.1016/j.ejvs.2020.02.023

[16] Sarantides, P., Raptis, A., Mathioulakis, D., Moulakakis, K., Kakisis, J., & Manopoulos, C. (2024). Computational Study of Abdominal Aortic Aneurysm Walls Accounting for Patient-Specific Non-Uniform Intraluminal Thrombus Thickness and Distinct Material Models: A Pre- and Post-Rupture Case. Bioengineering (Basel, Switzerland), 11(2), 144. https://doi.org/10.3390/bioengineering11020144

[17] Encord. (n.d.) DICOM vs. NIfTI: A comparison of medical imaging formats. https://encord.com/blog/dicom-and-nifti-comparison/

[18] European Parliament and Council. (2016). Regulation (EU) 2016/679 of the European Parliament and of the Council of 27 April 2016 on the protection of natural persons with regard to the processing of personal data and on the free movement of such data (General Data Protection Regulation). Official Journal of the European Union, L119, 1–88. https://eur-lex.europa.eu/eli/reg/2016/679/oj

[19] U.S. Department of Health and Human Services. (1996). Health Insurance Portability and Accountability Act of 1996 (HIPAA), Public Law 104-191. https://www.govinfo.gov/content/pkg/PLAW-104publ191/pdf/PLAW-104publ191.pdf

[20] Gonzalez, R. C., & Woods, R. E. (2018). Digital Image Processing (4ª ed.). Pearson.

[21] Pham, D. L., Xu, C., & Prince, J. L. (2000). Current methods in medical image segmentation. Annual review of biomedical engineering, 2, 315–337. https://doi.org/10.1146/annurev.bioeng.2.1.315

[22] Ronneberger, O., Fischer, P., Brox, T. (2015). U-Net: Convolutional Networks for Biomedical Image Segmentation. Medical Image Computing and Computer-Assisted Intervention – MICCAI 2015. MICCAI 2015. Lecture Notes in Computer Science(), vol 9351. Springer, Cham. https://doi.org/10.1007/978-3-319-24574-4_28

[23] Gillies, R. J., Kinahan, P. E., & Hricak, H. (2016). Radiomics: Images Are More than Pictures, They Are Data. Radiology, 278(2), 563–577. https://doi.org/10.1148/radiol.2015151169

[24] Rengier, F., Mehndiratta, A., von Tengg-Kobligk, H. et al. (2010). 3D printing based on imaging data: review of medical applications. International journal of computer assisted radiology and surgery, 5(4), 335–341. https://doi.org/10.1007/s11548-010-0476-x

[25] Georgakarakos, E., Ioannou, C. V., Volanis, S. et al. (2009). The influence of intraluminal thrombus on abdominal aortic aneurysm wall stress. International angiology : a journal of the International Union of Angiology, 28(4), 325–333.

[26] Tomaszewski, M. R., & Gillies, R. J. (2021). The Biological Meaning of Radiomic Features. Radiology, 298(3), 505–516. https://doi.org/10.1148/radiol.2021202553

[27] Abbasian Ardakani, A., Bureau, N. J., Ciaccio, E. J., & Acharya, U. R. (2022). Interpretation of radiomics features-A pictorial review. Computer methods and programs in biomedicine, 215, 106609. https://doi.org/10.1016/j.cmpb.2021.106609

[28] Litjens, G., Kooi, T., Bejnordi, B. E. et al. (2017). A survey on deep learning in medical image analysis. Medical image analysis, 42, 60–88. https://doi.org/10.1016/j.media.2017.07.005

[29] Lederle, F. A., Wilson, S. E., Johnson, G. R. et al. (1995). Variability in measurement of abdominal aortic aneurysms. Abdominal Aortic Aneurysm Detection and Management Veterans Administration

Cooperative Study Group. *Journal of vascular surgery*, *21*(6), 945–952. https://doi.org/10.1016/s0741-5214(95)70222-9

[30] Moll, F. L., Powell, J. T., Fraedrich, G. et al. (2011). Management of abdominal aortic aneurysms clinical practice guidelines of the European society for vascular surgery. *European journal of vascular and endovascular surgery : the official journal of the European Society for Vascular Surgery*, *41 Suppl 1*, S1–S58. https://doi.org/10.1016/j.ejvs.2010.09.011

[31] Singh, T. P., Moxon, J. V., Gasser, T. C. et al. (2023). Association between aortic peak wall stress and rupture index with abdominal aortic aneurysm-related events. *European radiology*, *33*(8), 5698–5706. https://doi.org/10.1007/s00330-023-09488-1

[32] Zhang, H., Kheyfets, V. O., & Finol, E. A. (2013). Robust infrarenal aortic aneurysm lumen centerline detection for rupture status classification. *Medical engineering & physics*, *35*(9), 1358–1367. https://doi.org/10.1016/j.medengphy.2013.03.005

[33] Debono, S., Tzolos, E., Syed, M. B. J. et al. (2024). CT Attenuation of Periaortic Adipose Tissue in Abdominal Aortic Aneurysms. *Radiology. Cardiothoracic imaging*, *6*(1), e230250. https://doi.org/10.1148/ryct.230250

[34] Aggarwal, S., Qamar, A., Sharma, V., & Sharma, A. (2011). Abdominal aortic aneurysm: A comprehensive review. Experimental and clinical cardiology, 16(1), 11–15.

[35] Rengier, F., Weber, T. F., Giesel, F. L. et al. (2012). Centerline analysis of aortic CT angiographic examinations: Benefits and limitations. *American Journal of Roentgenology, 192*(5), 131-140. https://doi.org/10.2214/AJR.08.1488

[36] Hinchliffe, R. J., Alric, P., Rose, D. et al. (2003). Comparison of morphologic features of intact and ruptured aneurysms of infrarenal abdominal aorta. *Journal of Vascular Surgery, 38*(1), 88-92. https://doi.org/10.1067/mva.2003.258

[37] Bodur, O., Grady, L., Stillman, A. et al. (2007). Semi-automatic aortic aneurysm analysis. In *Medical Imaging 2007: Physiology, Function, and Structure from Medical Images* (Vol. 6511, p. 65111G). https://doi.org/10.1117/12.710719

[38] Tang, A., Kauffmann, C., Tremblay-Paquet, S. et al. (2014). Morphologic evaluation of ruptured and symptomatic abdominal aortic aneurysm by three-dimensional modeling. *Journal of Vascular Surgery, 59*(4), 894–902. https://doi.org/10.1016/j.jvs.2013.10.097

[39] Liu, Q., Jiang, P., Jiang, Y., Ge, H., Li, S., Jin, H., & Li, Y. (2019). Prediction of Aneurysm Stability Using a Machine Learning Model Based on PyRadiomics-Derived Morphological Features. *Stroke*, *50*(9), 2314–2321. https://doi.org/10.1161/STROKEAHA.119.025777

[40] Zakeri, M., Atef, A., Aziznia, M., & Jafari, A. (2024). A comprehensive investigation of morphological features responsible for cerebral aneurysm rupture using machine learning. *Scientific reports*, *14*(1), 15777. https://doi.org/10.1038/s41598-024-66840-1

[41] Ludwig, C. G., Lauric, A., Malek, J. A., Mulligan, R., & Malek, A. M. (2021). Performance of Radiomics derived morphological features for prediction of aneurysm rupture status. *Journal of neurointerventional surgery*, *13*(8), 755–761. https://doi.org/10.1136/neurintsurg-2020-016808

[42] Patterson, B. O., Hinchliffe, R. J., Holt, P. J. et al. (2010). Importance of aortic morphology in planning aortic interventions. *Journal of endovascular therapy: an official journal of the International Society of Endovascular Specialists*, *17*(1), 73–77. https://doi.org/10.1583/09-2967C.1

[43] Wadgaonkar, A. D., Black, J. H., 3rd, Weihe, E. K. et al. (2015). Abdominal aortic aneurysms revisited: MDCT with multiplanar reconstructions for identifying indicators of instability in the pre- and postoperative patient. *Radiographics : a review publication of the Radiological Society of North America, Inc*, *35*(1), 254–268. https://doi.org/10.1148/rg.351130137

[44] Buijs, R. V., Willems, T. P., Tio, R. A. et al. (2013). Calcification as a risk factor for rupture of abdominal aortic aneurysm. *European journal of vascular and endovascular surgery: the official journal of the European Society for Vascular Surgery*, *46*(5), 542–548. https://doi.org/10.1016/j.ejvs.2013.09.006

[45] O'Leary, S. A., Mulvihill, J. J. et al. (2015). Determining the influence of calcification on the failure properties of abdominal aortic aneurysm (AAA) tissue. *Journal of the mechanical behavior of biomedical materials*, *42*, 154–167. https://doi.org/10.1016/j.jmbbm.2014.11.005

[46] Klopf, J., Fuchs, L., Schernthaner, R. et al. (2022). The prognostic impact of vascular calcification on abdominal aortic aneurysm progression. *Journal of vascular surgery*, *75*(6), 1926–1934. https://doi.org/10.1016/j.jvs.2021.11.062

[47] Rezaeitaleshmahalleh, M., Mu, N., Lyu, Z. et al. (2023). Radiomic-based Textural Analysis of Intraluminal Thrombus in Aortic Abdominal Aneurysms: A Demonstration of Automated Workflow. *Journal of cardiovascular translational research*, *16*(5), 1123–1134. https://doi.org/10.1007/s12265-023-10404-7

[48] Lv, R., Hu, G., Zhang, S. et al. (2024). Assessing abdominal aortic aneurysm growth using radiomic features of perivascular adipose tissue after endovascular repair. *Insights into imaging*, *15*(1), 232. https://doi.org/10.1186/s13244-024-01804-7

[49] Wang, Y., Xiong, F., Leach, J. et al. (2023). Contrast-enhanced CT radiomics improves the prediction of abdominal aortic aneurysm progression. *European radiology*, *33*(5), 3444–3454. https://doi.org/10.1007/s00330-023-09490-7

[50] Martínez-Muñoz, S., Ruiz-Fernandez, D., & Galiana-Merino, J. J. (2016). Automatic abdominal aortic aneurysm segmentation in MR images. *Expert Systems with Applications. 54, 78-87. doi:10.1016/j.eswa.2016.01.017*

[51] Lareyre, F., Adam, C., Carrier, M., Dommerc, C., Mialhe, C., & Raffort, J. (2019). A fully automated pipeline for mining abdominal aortic aneurysm using image segmentation. *Scientific reports*, *9*(1), 13750. https://doi.org/10.1038/s41598-019-50251-8

[52] Abdolmanafi, A. et al. (2023). Deep-learning method for fully automatic segmentation of the abdominal aortic aneurysm from computed tomography imaging. *Frontiers in cardiovascular medicine*, *9*, 1040053. https://doi.org/10.3389/fcvm.2022.1040053

[53] Mu, N., Lyu, Z., Rezaeitaleshmahalleh, M., Zhang, X., Rasmussen, T., McBane, R., & Jiang, J. (2023). Automatic segmentation of abdominal aortic aneurysms from CT angiography using a context-aware cascaded U-Net. *Computers in biology and medicine*, *158*, 106569. https://doi.org/10.1016/j.compbiomed.2023.106569

[54] Caradu, C., Spampinato, B., Vrancianu, A. M. et al. (2021). Fully automatic volume segmentation of infrarenal abdominal aortic aneurysm computed tomography images with deep learning approaches versus physician controlled manual segmentation. *Journal of vascular surgery*, *74*(1), 246–256.e6. https://doi.org/10.1016/j.jvs.2020.11.036

[55] Sieren, M. M., Widmann, C. et al. (2022). Automated segmentation and quantification of the healthy and diseased aorta in CT angiographies using a dedicated deep learning approach. *European radiology*, *32*(1), 690–701. https://doi.org/10.1007/s00330-021-08130-2

[56] Joldes, G. R., Miller, K., Wittek, A. et al. (2017). BioPARR: A software system for estimating the rupture potential index for abdominal aortic aneurysms. *Scientific reports*, 7(1), 4641. https://doi.org/10.1038/s41598-017-04699-1

[57] Fedorov, A. et al. (2012). 3D Slicer as an image computing platform for the Quantitative Imaging Network. *Magnetic resonance imaging*, 30(9), 1323–1341. https://doi.org/10.1016/j.mri.2012.05.001

[58] Materialise. *Mimics Innovation Suite*. https://www.materialise.com/en/healthcare/mimics

[59] van Griethuysen, J. J. M., Fedorov, A., Parmar, C. et al. (2017). Computational Radiomics System to Decode the Radiographic Phenotype. *Cancer research*, 77(21), e104–e107. https://doi.org/10.1158/0008-5472.CAN-17-0339

[60]   US8781193B2   *- Automatic   quantitative   vessel analysis*. https://patents.google.com/patent/US8781193B2/en

[61]   CN104619244B   *- Noninvasive   systems   for   aortic   aneurysm evaluation*. https://patents.google.com/patent/CN104619244B/en

[62] WO2010121146A2 *- Aneurysm detection*. https://patents.google.com/patent/WO2010121146A2/en

[63] *AneuPy: An open-source tool for simulation-ready AAA geometries*. https://arxiv.org/abs/2504.15285

[64] Gobierno de España. (2018). *Organic Law 3/2018, of 5 December, on the Protection of Personal Data and guarantee of digital rights*. https://www.boe.es/buscar/act.php?id=BOE-A-2018-16673

[65] World Medical Association. (2013). *Declaration of Helsinki – Ethical Principles for Medical Research Involving Human Subjects*. https://www.wma.net/policies-post/wma-declaration-of-helsinki-ethical-principles-for-medical-research-involving-human-subjects/

[66] European Parliament & Council of the European Union. (2017). *Regulation (EU) 2017/745 on medical devices*. https://eur-lex.europa.eu/eli/reg/2017/745/oj

[67] International Organization for Standardization. (2016). *ISO 13485:2016: Medical devices – Quality management systems – Requirements for regulatory purposes*.

[68] International Organization for Standardization. (2013). *ISO/IEC 27001:2013: Information technology – Security techniques – Information security management systems – Requirements*.

[69] International Organization for Standardization. (2015). *ISO 9001:2015: Quality management systems – Requirements*.

15. ANNEXES

ANNEX 1: GitHub repository

All the code implemented in this project can be found in a public GitHub repository. Specifically in the *pipeline* folder, which contains four main scripts:

▪ **utils.py**: contains all the functions defined, which are imported and used by the other two scripts.

▪ **process_patient.py**: contains a function that extracts all the features, both morphological and radiomic, for a single acquisition of a single patient. It uses as inputs the segmentation (*.nrrd*) and the image (*.nii*) files.

▪ **run_single_patient.py**: executes the *process_patient* script two times for each patient (both acquisitions) and generates all the result tables and medical report.

▪ **report_template.qmd**: quarto template that is executed by *run_single_patient.py* and automatically generates a pdf medical report stored in the base directory.

GitHub reference:

Juliaviladelgado.   GitHub   –   juliaviladelgado/TFG_AAA_Analysis.
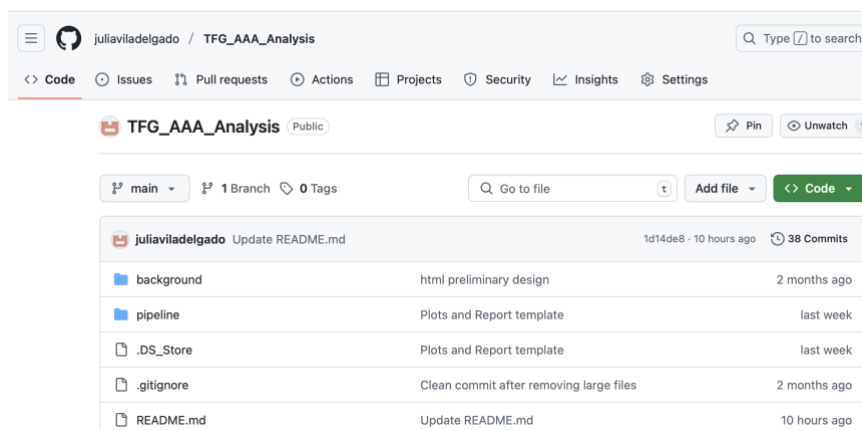https://github.com/juliaviladelgado/TFG_AAA_Analysis

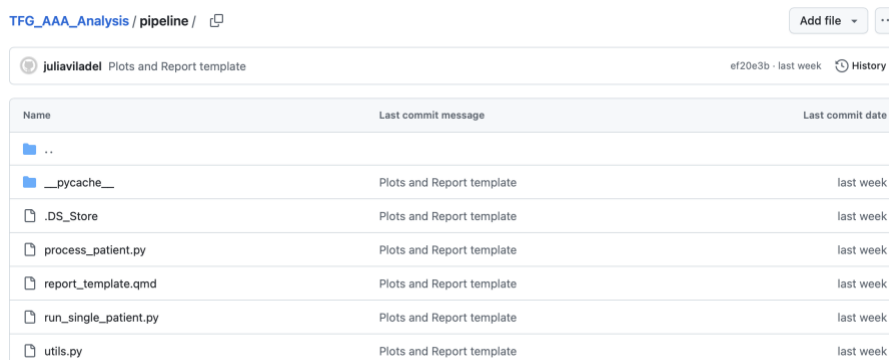*Figure 39: Screenshot of the public GitHub repository containing the full code of the project.*

Figure 40: Screenshot of the main files inside the "pipeline" folder.

ANNEX 2: Cross-sectional area computation

In this annex, a detailed explanation of the code segment responsible for extracting transversal areas is provided, given its length and multiple components, which could not be fully addressed in the main text.

In some sections of the abdominal aorta, especially where the vessels are highly curved, a simple cross-sectional slice can intersect multiple disconnected or partially connected structures. This occurs because the slicing plane may cross two nearby parts of the vessel wall or adjacent branches in the same 2D frame. As a result, the raw intersection can contain several unconnected or ambiguous components, compromising the accuracy of transversal area measurements. To address this, the function *get_main_island_mask()* was implemented. It performs 2D slicing operation over a 3D binary mask and automatically isolates the main structure of interest in the resulting slice, based on its proximity to the centerline and morphological processing. Then, since this mask is deformed due to all the process, it is only used as mask to constrain the real cross-sectional areas of the different segments (lumen, thrombus, wall, calcifications).
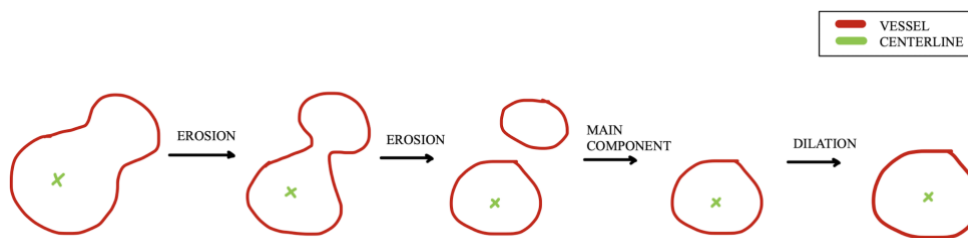

Figure 41: Representation of the process to obtain main component of a binary mask.

Below is a step-by-step explanation of the function logic.

Step 1: The function starts by extracting the voxel spacing and physical origin from the image header. This is necessary to convert between physical space (mm) and voxel coordinates.

```
350     # FUNCTION TO GET MAIN ISLAND OF A 2D SLICE FROM A MASK
351
352 ∨  def get_main_island_mask(binary_mask, point, normal, header, grid_size=500, resolution=0.5):
372         # 1. Extract voxel spacing and image origin from header
373         directions_mat = header["space directions"][1:]
374         directions = np.array([directions_mat[0][0], directions_mat[1][1], directions_mat[2][2]])
375         origin = np.array(header["space origin"])
```

Step 2: A square 2D grid is created, centered at the input point, and lying on the plane orthogonal to the normal vector. This grid will be used to resample the 3D image.

```
380         # 2. Create a 2D grid in the plane orthogonal to the normal vector
381         side_length = int(grid_size / resolution)
382         x = np.linspace(-grid_size / 2, grid_size / 2, side_length)
383         y = np.linspace(-grid_size / 2, grid_size / 2, side_length)
384         xv, yv = np.meshgrid(x, y)
```

Step 3: To define the slicing plane, two orthonormal vectors (v1, v2) perpendicular to the normal are computed, which define the axes of the 2D plane on which the cross-section is generated.

```
386         # 3. Define in-plane orthonormal basis vectors
387         v1 = np.array([-normal[1], normal[0], 0])
388         if np.linalg.norm(v1) < 1e-3:
389             v1 = np.array([0, -normal[2], normal[1]])
390         v1 = v1 / np.linalg.norm(v1)
391         v2 = np.cross(normal, v1)
```

Step 4 & 5: Using the grid and the vectors defined above, the 3D physical coordinates of each pixel in the slicing plane are calculated and converted into voxel indices.

```
393         # 4. Compute the 3D coordinates for every point in the 2D slicing plane
394         coords = (point[:, np.newaxis, np.newaxis] +
395                   v1[:, np.newaxis, np.newaxis] * xv +
396                   v2[:, np.newaxis, np.newaxis] * yv)
397
398         # 5. Convert those physical coordinates to voxel indices
399         coords_vox = (coords - origin[:, np.newaxis, np.newaxis]) / directions[:, np.newaxis, np.newaxis]
400
```

Step 6 & 7: The binary 3D mask is sampled over the 2D plane using nearest-neighbor interpolation. This results in a binary 2D image representing the intersection of the 3D structure with the plane. If the resulting slice is empty (no intersecting structure is present), the function returns an empty mask immediately.

```
401         # 6. Interpolate the 3D binary mask over this 2D plane (nearest-neighbor)
402         slice_vals = map_coordinates(binary_mask, coords_vox, order=0, mode='constant', cval=0.0)
403         slice_binary = slice_vals > 0
404
405         # 7. Return an empty mask if there's no structure in the slice
406         if np.sum(slice_binary) == 0:
407             return np.zeros_like(slice_binary, dtype=bool)
```

Step 8: To separate touching or slightly connected components, iterative binary erosion is applied. This continues until at least two disconnected components appear, or a maximum number of iterations is reached. This helps resolving ambiguities where two vessel segments are artificially joined.

```
409         # 8. Apply progressive erosion until we get >=2 components or max iterations reached
410         current_mask = slice_binary.copy()
411         max_iter = 20
412         performed_iterations = 0
413         eroded_empty = False
414
415         structure = disk(1)
416
417         for i in range(1, max_iter + 1):
418             eroded = binary_erosion(current_mask, structure=structure)
419             if np.sum(eroded) == 0:
420                 eroded_empty = True  # erosion completely removed the structure
421                 break
422             labeled_tmp, num_labels = label(eroded)
423             performed_iterations = i
424             current_mask = eroded
425             if num_labels >= 2:
426                 break
```

Step 9: If erosion completely removes the mask (especially in small slices), the function falls back to using the original slice.

```
428        # 9. Fallback if erosion removed everything → revert to original mask
429        if eroded_empty or performed_iterations == 0:
430            labeled, _ = label(slice_binary)
431            used_mask = slice_binary
432            performed_iterations = 0
433        else:
434            labeled, _ = label(current_mask)
435            used_mask = current_mask
```

Step 10: The mask is labeled to identify all non-background connected components (also known as "islands").

```
437        # 10. Get all non-background labels
438        labels_present = np.unique(labeled)
439        labels_present = labels_present[labels_present != 0]
440        if len(labels_present) == 0:
441            return np.zeros_like(slice_binary, dtype=bool)
```

Step 11: For each connected component (or "island") detected in the slice, its centroid is computed. Since the slicing plane is defined to pass through a specific point on the centerline, the relevant anatomical structure is expected to lie near the center of the image. Therefore, the component whose centroid is closest to the center of the 2D slice is selected as the main structure, since it is the one that will be intersecting with the centerline.

```
443        # 11. Find the component whose centroid is closest to the image center
444        center_pixel = np.array([side_length // 2, side_length // 2])
445        min_dist = np.inf
446        best_label = None
447        for lbl in labels_present:
448            com = np.array(center_of_mass(labeled == lbl))
449            dist = np.linalg.norm(com - center_pixel)
450            if dist < min_dist:
451                min_dist = dist
452                best_label = lbl
453
454        main_component = labeled == best_label
```

Step 12: The selected component is dilated using the same number of erosion iterations previously performed. This approximates the original size of the structure but now with improved separation from unwanted segments.

```
456        # 12. Dilate back to approximate original size using same number of iterations as erosion
457        restored_mask = binary_dilation(main_component, structure=structure, iterations=performed_iterations)
458
459        return restored_mask
```

Then, this mask is used as constrain to determine the cross-sections of the individual segments, excluding the pixels that belong to unwanted regions.

ANNEX 3: Contact area computation function

In order to quantify the contact surface between the ILT and the aortic wall, a surface-based geometric approach is applied. This method identifies the areas of the thrombus surface that lie in close proximity to the wall surface, based on the assumption that such proximity indicates anatomical contact.

Step 0: To perform surface-based analysis, the binary masks of both the thrombus and the wall are first converted into 3D triangular meshes. This is done using the function *generate_mask_from_mesh( ),* which follows these steps:

- Applies gaussian smoothing to the binary mask to reduce noise in jagged edges.
- Uses the **Marching Cubes** algorithm (from the *skimage.measure* module) to extract an isosurface corresponding to the anatomical boundary.
- Converts the vertices from voxel coordinates to physical space using image metadata.
- Applies laplacian smoothing to improve surface regularity using PyVista's *.smooth( )* method.

This results in two smooth *pv.PolyData* meshes: one for the thrombus and one for the wall.

```
789  def generate_mesh_from_mask(binary_mask, header, sigma=0.6, threshold=0.5, n_iter=100, relaxation=0.05):
790      """
791      Generates a smoothed 3D mesh from a binary mask using Gaussian filtering and marching cubes.
792
793      Args:
794          binary_mask (np.ndarray): 3D binary mask of the structure.
795          header (dict): NRRD/NIfTI-style header with 'space directions' and 'space origin'.
796          sigma (float): Standard deviation for Gaussian smoothing.
797          threshold (float): Threshold value to binarize the smoothed mask.
798          n_iter (int): Number of iterations for Laplacian smoothing.
799          relaxation (float): Relaxation factor for Laplacian smoothing.
800
801      Returns:
802          pv.PolyData: Smoothed PyVista mesh in physical space (mm).
803      """
804      # 1. Gaussian smoothing
805      smooth_mask = gaussian_filter(binary_mask.astype(float), sigma=sigma)
806      binary_smooth = smooth_mask > threshold
807
808      # 2. Marching cubes
809      verts, faces, normals, values = measure.marching_cubes(binary_smooth, level=0.5)
810
811      # 3. Convert to physical space
812      verts_mm = voxel_to_world_coords(verts, header)
813
814      # 4. Convert faces to PyVista format
815      faces_pv = np.hstack([[3, *face] for face in faces])
816
817      # 5. Create PyVista mesh
818      mesh = pv.PolyData(verts_mm, faces_pv)
819
820      # 6. Apply Laplacian smoothing
821      mesh_smooth = mesh.smooth(n_iter=n_iter, relaxation_factor=relaxation)
822
823      return mesh_smooth
```

Step 1: To efficiently compute the distances between surfaces, a KDTree is built using the coordinates of all points on the wall mesh. This structure allows fast nearest-neighbor queries for each triangle of the thrombus mesh.

```
834      # FUNCTION TO COMPUTE THE CONTACT AREA BETWEEN TWO MESHES
835  ∨  def compute_contact_area_from_meshes(thrombus_mesh, wall_mesh, distance_threshold=1.0):
851          # Step 1: Build a KDTree for efficient nearest-neighbor queries on wall mesh points
852          wall_points = wall_mesh.points
853          tree = cKDTree(wall_points)
```

Step 2: The function loops over each triangle in the thrombus mesh:

- For each triangle, it retrieves the three vertices and calculates the centroid (geometric center).
- Then, it queries the KDTree to find the minimum distance from this centroid to any point on the wall mesh.

If the centroid of a triangle is within a predefined distance threshold to the wall, the triangle is considered to be in contact. The area of such a triangle is computed using the vector cross product formula:

$$Area = \frac{1}{2} \cdot \|(p_1 - p_0) \times (p_2 - p_0)\|$$

Equation 5: :Area of a triangle computed using the vector cross product formula.

The area is then added to the running total of contact area and the function returns two ouptuts:

- The total estimated contact area (in mm^2).
- The indices of triangles in contact, which have been used for visual validation.

```
858          # Step 2: Iterate over all triangles in the thrombus mesh
859          for i, face in enumerate(thrombus_mesh.faces.reshape(-1, 4)):
860              assert face[0] == 3  # Ensure this is a triangle (PyVista format)
861
862              # Get the vertex indices and positions for the triangle
863              idx0, idx1, idx2 = face[1], face[2], face[3]
864              p0, p1, p2 = thrombus_mesh.points[[idx0, idx1, idx2]]
865
866              # Compute the centroid of the triangle
867              centroid = (p0 + p1 + p2) / 3.0
868
869              # Find the distance to the nearest point on the wall mesh
870              distance, _ = tree.query(centroid)
871
872              # If the centroid is close enough to the wall, consider it in contact
873              if distance <= distance_threshold:
874                  area = triangle_area(p0, p1, p2)  # Compute area of the triangle
875                  contact_area += area             # Accumulate contact area
876                  contact_faces.append(i)          # Save the triangle index
877
878          return contact_area, contact_faces
```
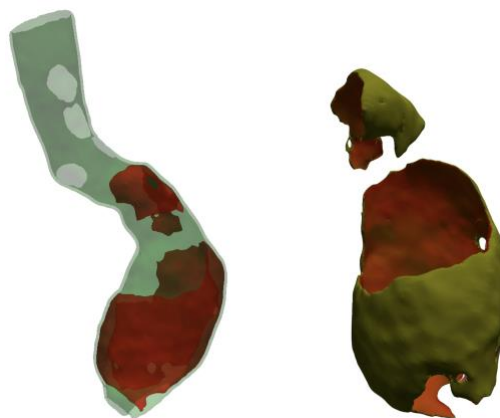

Figure 42: Visual validation of the contact area between the thrombus and wall.

ANNEX 4: Example of a medical report automatically generated

In this annex, some screenshots of some part of the medical report automatically generated can be visualized. A complete medical report example can be found on the public GitHub repository (*Annex 1*).

Patient's Medical Report

SP5021

General Overview

This report summarizes morphological metrics of the aorta and associated structures.

Summary of parameter evolution

	Feature	Value T1	Value T2	% of Change
0	Diameter Max LT (mm)	50.636726	60.936838	20.341187
1	Diameter Max V (mm)	53.575548	64.012187	19.480229
2	Diameter Median SRA (mm)	24.360491	24.346870	-0.055917
3	Diameter ratio IRA/SRA	2.078641	2.502861	20.408516
4	Transversal Area Median LT (mm²)	505.875000	577.375000	14.133926
5	Transversal Area Std LT (mm²)	507.548490	846.289711	66.740662
6	Circularity Median Lumen	0.980662	0.969571	-1.130945
7	Circularity Std Lumen	0.031656	0.031593	-0.200350
8	Circularity Median Lumen+Thrombus	0.990257	0.985940	-0.435949
9	Circularity Std Lumen+Thrombus	0.012642	0.014078	11.359003
10	Tortuosity	1.187730	1.229894	3.549948
11	Contact Area Thrombus-Wall (mm²)	8800.932829	12288.468892	39.626891
12	Thrombus/Lumen Ratio IRA	0.441950	0.790559	78.879790
13	Lumen/Lumen_Thrombus Ratio IRA	0.693506	0.558485	-19.469284
14	Number of Calcifications	79.000000	83.000000	5.063291
15	Average Calcification Volume (mm³)	32.862908	41.136684	25.176642
16	Total Calcification Volume (mm³)	5192.339401	6828.689575	31.514700

Table 1: This table summarizes all relevant parameters evolution showing the relative changes across the two acquisitions. Abbreviations: LT (Lumen + Thrombus), V (Vessel), IRA/SRA (Inferior/Superior Renal Aorta).
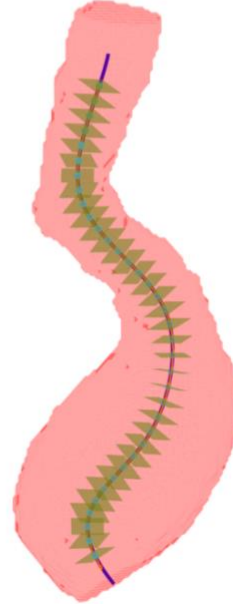
Aorta Visualization

Below, a comparative visualization for **T1** and **T2** acquisitions is presented. The images show the **3D segmentation** with the **sampled points** and the **transversal planes** defined at each step. This is shown for both acquisitions.

T1 - 3D Segmentation, Centerline & Transversal Planes
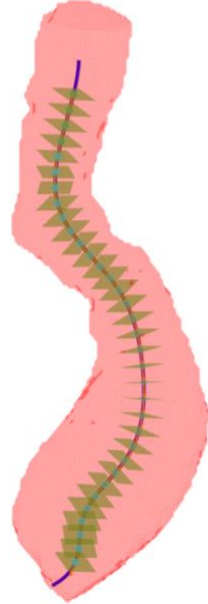
T2 - 3D Segmentation, Centerline & Transversal Planes

Evolution of Transversal Areas

The following plots illustrate the evolution of the transversal areas along the centerline for **T1** and **T2** acquisitions. A table summarizes the **median** and **standard deviation** of the transversal area of the **lumen + thrombus** segment (LT) and their relative change.

T1 - Evolution of Transversal Areas
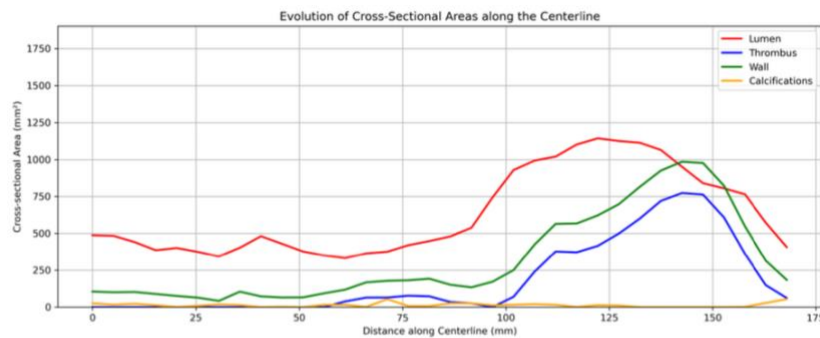
## T2 - Evolution of Transversal Areas
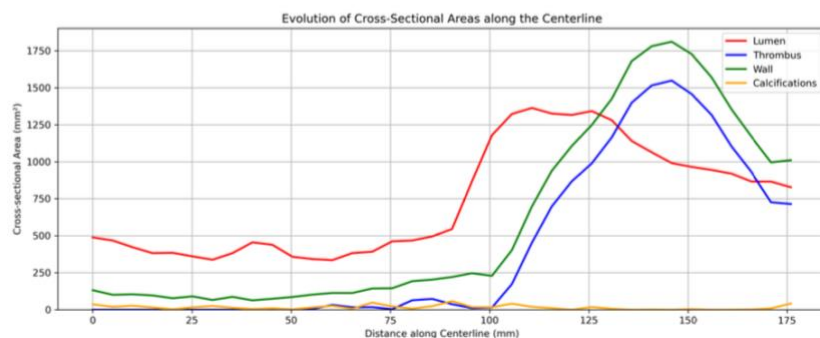
	Feature	Value T1	Value T2	% of Change
4	Transversal Area Median LT (mm²)	505.87500	577.375000	14.133926
5	Transversal Area Std LT (mm²)	507.54849	846.289711	66.740662

Table 2: Table summarizing cross-sectional area ratios. Abbreviations: LT (Lumen + Thrombus).

Evolution of Maximum Diameters

Below, the evolution of **maximum diameters** along the centerline is shown for **T1** and **T2** acquisitions, along with key diameter-related metrics.
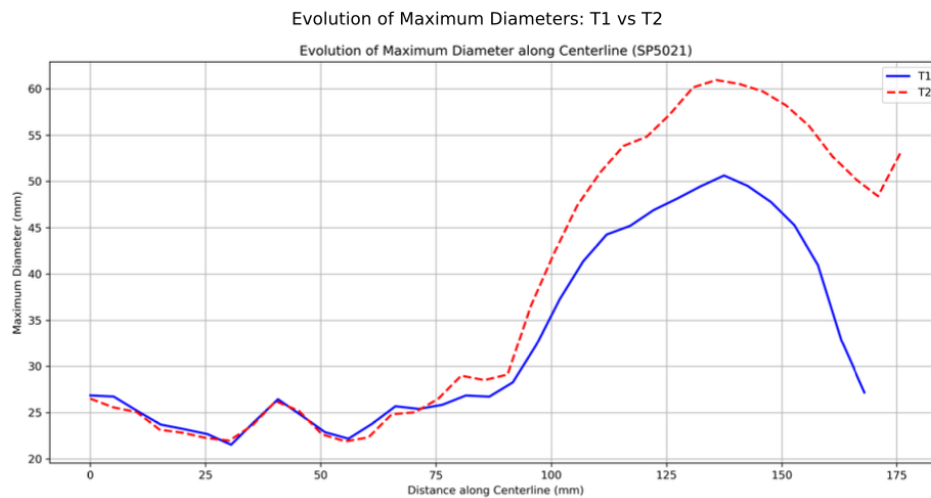

Evolution of Maximum Diameters: T1 vs T2

	Feature	Value T1	Value T2	% of Change
0	Diameter Max LT (mm)	50.636726	60.936838	20.341187
1	Diameter Max V (mm)	53.575548	64.012187	19.480229
2	Diameter Median SRA (mm)	24.360491	24.346870	-0.055917
3	Diameter ratio IRA/SRA	2.078641	2.502861	20.408516

Table 3: Table summarizing diameter measures. Abbreviations: LT (Lumen + Thrombus), V (Vessel, including all structures), IRA/SRA (Inferior/Superior Renal Aorta).

Evolution of segment volumes

Below, the 3D meshes of the lumen, thrombus, and calcifications are visualized separately in the last figure. Before that, the **combined meshes** of these structures are displayed in anterior and posterior views for both **T1** and **T2** acquisitions. Finally, the table summarizes the **evolution of the volumes** for each segment and relevant ratios.
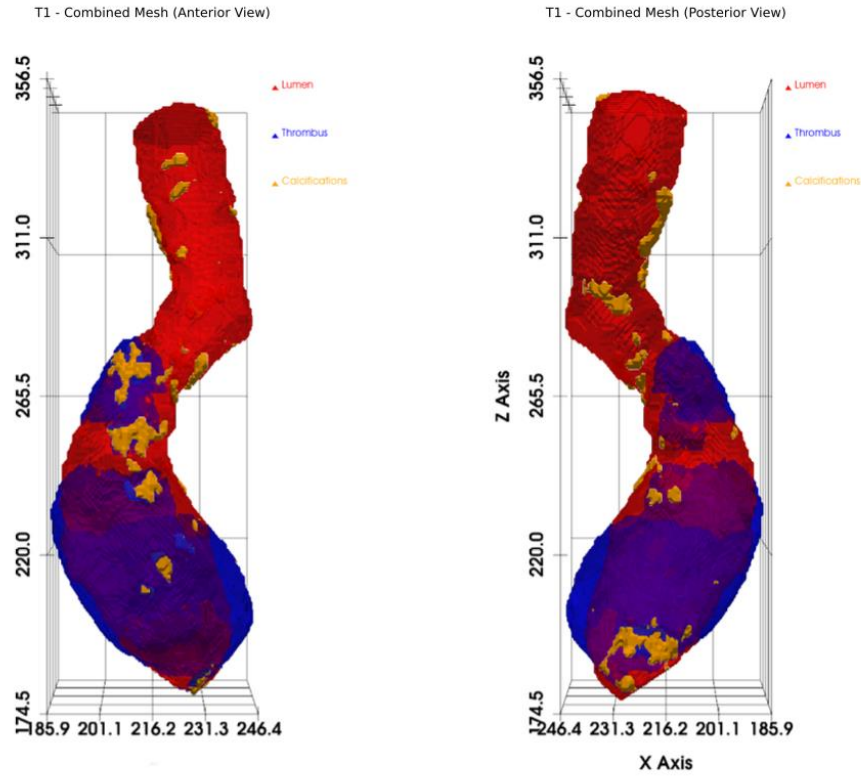
	Feature	Value T1	Value T2	% of Change
12	Thrombus/Lumen Ratio IRA	0.441950	0.790559	78.879790
13	Lumen/Lumen_Thrombus Ratio IRA	0.693506	0.558485	-19.469284

Table 4: Table volume ratios. Abbreviations: IRA (Inferior Renal Aorta).

	Feature (mm³)	T1	T2	% Change
0	Volume Lumen_IRA	84182.92	103433.79	22.87
1	Volume Thrombus_IRA	37204.61	81770.47	119.79
2	Volume Calcifications_IRA	1844.00	2250.22	22.03
3	Volume Wall_IRA	56576.98	108105.73	91.08
4	Volume Lumen_Thrombus_IRA	121387.53	185204.26	52.57
5	Volume Lumen_A	118489.45	136172.10	14.92
6	Volume Thrombus_A	37204.61	81770.47	119.79
7	Volume Calcifications_A	2596.17	3414.34	31.51
8	Volume Wall_A	63847.56	115886.11	81.50
9	Volume Lumen_SRA	34306.53	32738.31	-4.57
10	Volume Thrombus_SRA	0.00	0.00	NaN
11	Volume Calcifications_SRA	752.17	1164.12	54.77
12	Volume Wall_SRA	7270.58	7780.38	7.01

Table 5: Table with volume evolution for all segments. Abbreviations: IRA/SRA (Inferior/Superor Renal Aorta), A (Inferior + Superior Renal Aorta).

64

Curvature Plots and Tortuosity Evolution

The following table summarizes the **Tortuosity** evolution. Below, the evolution of the curvature of the centerline is presented for both **T1** (top) and **T2** (bottom) acquisitions.

	Feature	Value T1	Value T2	% of Change
10	Tortuosity	1.18773	1.229894	3.549948

Table 6: Table with centerline tortuosity evolution of the Lumen + Thrombus segment (dimensionless).
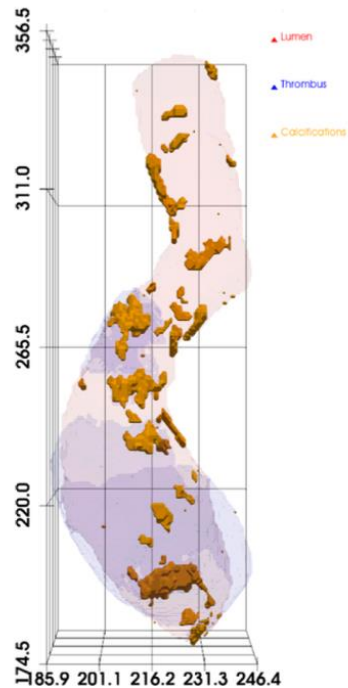
T1 - Curvature Plot (Lumen + Thrombus)
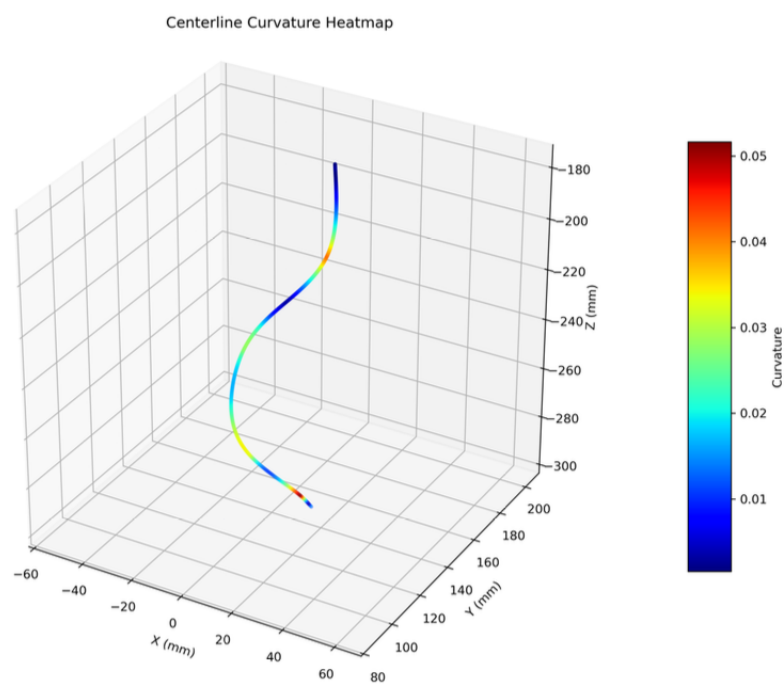
Evolution of Calcifications

This section presents the number, average volume, and total volume of **calcifications** for both acquisitions (T1 and T2) and their correspodning 3D visualization.

	Feature	Value T1	Value T2	% of Change
14	Number of Calcifications	79.000000	83.000000	5.063291
15	Average Calcification Volume (mm³)	32.862908	41.136684	25.176642
16	Total Calcification Volume (mm³)	5192.339401	6828.689575	31.514700

Table 7: Table summarizing calcification metrics evolution.